Phosphorylation Toggles the SARS-CoV-2 Nucleocapsid Protein Between Two Membrane-Associated Condensate States

Bruna Favetta[1], Huan Wang[2], Jasmine Cubuk[3], Arjun Singh[4], Mayur Barai[4], Cesar Ramirez[1], Adam J. Gormley[1], Sanjeeva Murthy[2], Gregory Dignon[4], Andrea Soranno[3], Zheng Shi[2], Benjamin S. Schuster[4]

1 Department of Biomedical Engineering, Rutgers, The State University of New Jersey, Piscataway, NJ 08854
2 Department of Chemistry and Chemical Biology, Rutgers, The State University of New Jersey, Piscataway, NJ 08854
3 Department of Biochemistry and Molecular Biophysics, Washington University in St Louis, St. Louis, MO 63110
4 Department of Chemical and Biochemical Engineering, Rutgers, The State University of New Jersey, Piscataway, NJ 08854

Corresponding author benjamin.schuster@rutgers.edu

Key Words: SARS-CoV-2, liquid-liquid phase separation (LLPS), phosphorylation, protein-RNA interactions, material properties, membrane interaction

Summary

The Nucleocapsid protein (N) of SARS-CoV-2 plays a critical role in the viral lifecycle by regulating RNA replication and packaging the viral genome. N and RNA phase separate to form condensates that may be important for these functions. Both functions occur at membrane surfaces, but how N toggles between these two membrane-associated functional states is unclear. Here, we reveal that phosphorylation switches how N condensates interact with membranes, partly by modulating condensate material properties. Phosphorylated N forms liquid condensates that wet membranes, reminiscent of N's role in RNA replication. In contrast, unmodified N forms viscoelastic condensates that can be engulfed by membranes, evoking viral genome packaging. These results suggest that phosphorylation serves as a regulatory switch within the viral replication cycle by modulating N's association with membranes. We gained mechanistic insight through structural analysis and molecular simulations, which suggest phosphorylation induces a conformational change that softens condensate material properties. Our studies also show that phosphorylation alters N's interaction with viral membrane proteins. Together, our findings uncover a novel aspect of SARS-CoV-2 biology by identifying membrane association as a key feature of N condensates and providing mechanistic insights into the regulatory role of phosphorylation. Understanding this mechanism suggests potential therapeutic targets for COVID infection.

Introduction

The COVID pandemic has focused attention on the mechanisms of SARS-CoV-2 viral replication. SARS-CoV-2 is an enveloped virus with a non-segmented, positive-sense, single-stranded, ~30 kb RNA genome[1]. In the virus core, genomic RNA (gRNA) is associated with Nucleocapsid protein (N), forming a ribonucleoprotein (RNP) complex. N has several functions during the viral life cycle but is primarily involved in protecting the viral RNA genome by binding, condensing, and packaging it within the virion[2]. N has also been shown to be necessary for

47 efficient transcription and replication of viral RNA, and it additionally contributes to immune
48 evasion via sequestering stress granule proteins[3]. How N is regulated throughout the viral lifecycle
49 to perform its varied functions, and whether it is possible to therapeutically manipulate this
50 regulation to inhibit viral replication, remains unknown.

51 N is a multi-domain protein, consisting of two folded and three disordered domains (Fig.
52 1A), the diversity of which likely contributes to its ability to perform several functions throughout
53 the viral lifecycle[2]. The N-terminal folded domain (NTD) strongly binds with specific viral RNA
54 elements, stabilizing the RNP complex[4,5]. The C-terminal folded domain (CTD) mediates
55 dimerization of N, facilitating the formation of the helical nucleocapsid structure that protects the
56 viral RNA genome[6,7]. Both folded domains are flanked by disordered regions. The central
57 disordered region acts as a linker that is partially extended and thus retains some structure while
58 providing the protein conformational flexibility[8,9]. The serine/arginine (SR)-rich region (aa 175 –
59 206; Fig. 1B) within the linker is known to participate in both protein–protein and protein–RNA
60 interactions[10–12].

61 Importantly, this SR-rich region was identified as a site of phosphorylation of N (Fig. 1B)
62 that may regulate protein function, based on several lines of evidence. 1) At different stages of
63 the viral life cycle, N exists in two phosphorylation states. Abundant phosphorylated protein is
64 found inside infected cells, while unmodified protein is found within virions[13–18]. Regulation of
65 phosphorylation of N may act as a timer in the viral lifecycle, switching from replication,
66 transcription, and translation to assembly of new virions[19–21]. 2) Phosphorylation of the SR-rich
67 region of N has been shown to modify how the protein interacts with RNA, as well as affect the
68 transcription and translation of RNA[22,23]. 3) During viral replication, when N is likely
69 phosphorylated, it appears to form a thin layer around viral replication organelles (vROs), double
70 membrane vesicles filled with viral RNA commonly found in infected cells[16,24]. However, during
71 virion assembly, complexes of unmodified N and RNA remain as small, spherical structures while
72 the viral capsid is engulfed by the ER-Golgi intermediate complex (ERGIC) membrane[25]. Although

73 little attention has been given to N's interactions with membranes, these observations suggest
74 that phosphorylation of N and its membrane interactions are linked and may underlie N's multiple
75 functions. The goal of this paper is to elucidate this link between N phosphorylation and its
76 membrane interaction at the molecular level, providing insights critical for understanding COVID
77 infection.

78 We sought to understand the phosphorylation-dependent membrane interactions of N
79 through the lens of phase separation. N contains RNA-binding and disordered domains, which
80 enable N and RNA to interact in a dynamic manner. This results in the formation of droplets
81 enriched in protein and RNA, known as biomolecular condensates[3,8,26,27]. N undergoes phase
82 separation with RNA in vitro and in vivo[28,29]; experiments show that phosphorylation of N[19,26], type
83 of RNA[30,31], and temperature[30] modulate the condensate's propensity to phase separate and
84 affect its molecular dynamics. Biomolecular condensates can display a range of material
85 properties, from liquids to gels, which may be closely associated with their function[32,33]. The
86 material properties of a condensate need not be static, and cellular regulation can modulate
87 material properties and thus condensate function[34]. Carlson et al. showed that unmodified N and
88 RNA form gel-like condensates and discrete 15-nm particles, while phosphorylated N generates
89 a more liquid-like droplet. They hypothesized that this difference in material properties could be
90 the basis for a dual role of N during the viral lifecycle in both regulating RNA transcription and
91 facilitating nucleocapsid assembly[35,36]. However, how the phosphorylation-dependent material
92 properties of N condensates affect their interaction with membranes has not been studied. Recent
93 investigations on condensate-membrane interaction show that condensate material properties
94 are a key factor determining the mode of interaction between condensates and the membrane
95 surface[37–39]. Based on this, we hypothesized that phosphorylation tunes how N and RNA interact,
96 thus modulating the material properties of N and RNA condensates, consequently influencing
97 condensate-membrane interaction, and in turn allowing N to display the two distinct behaviors
98 observed throughout the viral life cycle (Fig. 1C-D).

99 Here, we tested this hypothesis using careful in vitro reconstitutions to map how
100 condensates formed by N and viral RNA fragments interact with membranes. We identified
101 membrane association as a feature of N condensates, and we found that this interaction is
102 regulated at least in part by N's phosphorylation state. Unmodified N condensates retain their
103 shape upon interaction with membranes, but phosphorylation reduces condensate viscoelasticity,
104 such that phosphorylated N (pN) condensates are softer and therefore wet membrane surfaces.
105 Phosphorylation also switches N's ability to interact with viral membrane proteins. These results
106 provide a mechanism by which N can toggle between distinct membrane-associated functions.
107 To understand these changes at a molecular level, we performed structural studies and molecular
108 simulations that revealed that phosphorylation strengthens interactions between pN monomers
109 within pN dimers and thus weakens protein-RNA binding. We propose a model where
110 phosphorylation acts as a functional switch during the viral lifecycle, shifting N's roles from RNA
111 replication to virion assembly by toggling its membrane interaction.
112
113 **Results**
114 We reconstituted N or pN and RNA condensates in vitro. We prepared recombinantly
115 expressed N that was either kept unmodified or was phosphorylated in vitro using GSK-3β and
116 SRPK1 kinases[17] (Fig. 1B). Up to 9 phosphorylation sites on N were confirmed using mass
117 spectrometry and Phos-Tag SDS-PAGE (Supplementary Fig. 1). We used in vitro transcription to
118 make fragments of viral RNA that are known to promote phase separation of N (Fig. 1E)[30]. First,
119 we tested a fragment containing the first 1000 base pairs from the 5' end of the viral genome that
120 contains important regulatory information[1]. Second, we tested the fragment of RNA that encodes
121 N (containing the first 75 nucleotides of the 5′ untranslated region recombined onto the N protein
122 coding sequence), given that it is highly produced during viral infection[1]. As expected, mixing N
123 or pN protein with either RNA at 37°C resulted in their condensation into protein- and RNA-rich
124 droplets (Fig. 1F). A change in morphology with regards to the degree of sphericity of droplets

already suggests that condensates are modulated by both type of RNA and phosphorylation status of the protein (Supplementary Fig. 2), two factors that we investigate in depth.

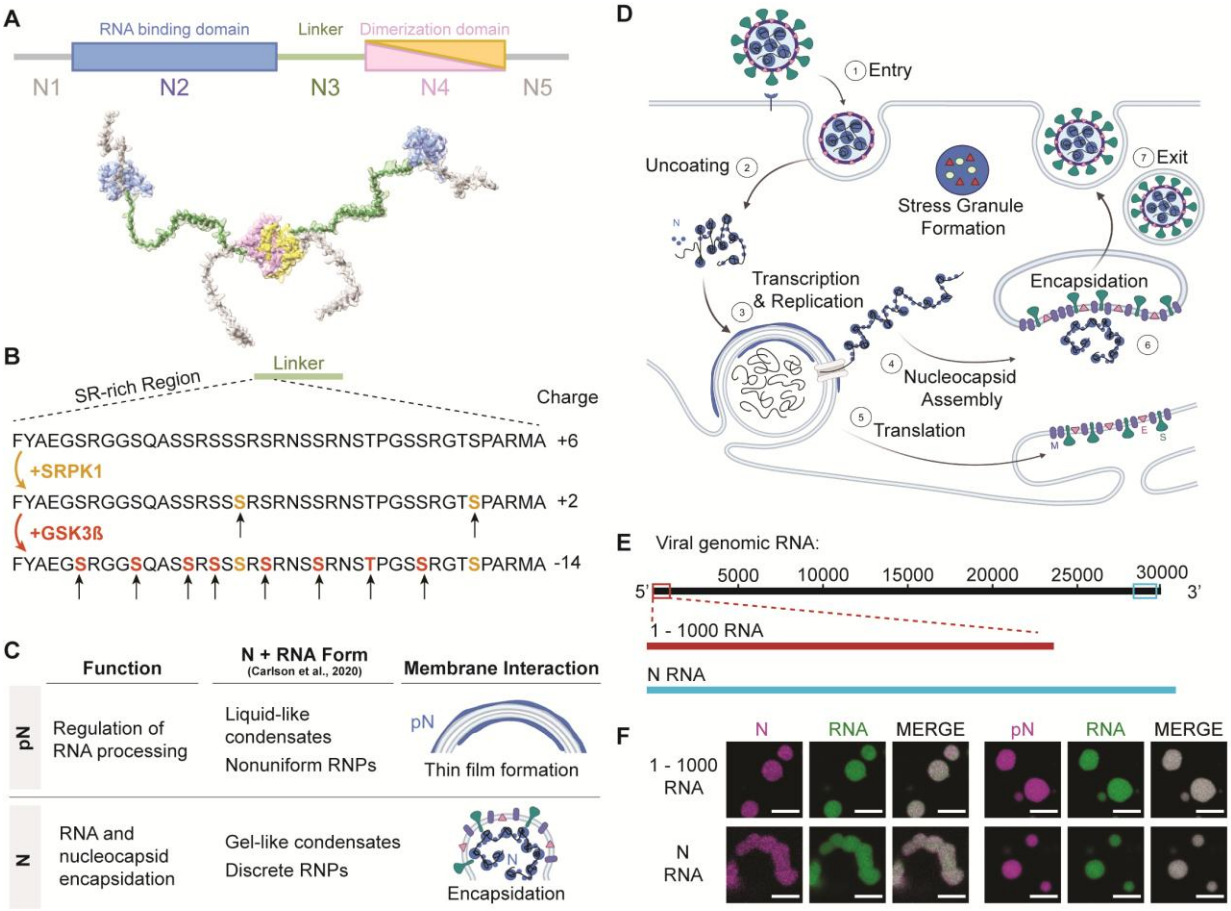

Figure 1: Phosphorylation of the SARS-CoV-2 Nucleocapsid protein (N). A) Schematic of full-length SARS-CoV-2 Nucleocapsid protein (N) used in experiments, showing N1, a disordered domain; N2, RNA binding domain (PDB ID: 7VBD); N3, disordered linker domain containing the Serine-Arginine-rich (SR) region; N4, dimerization domain (PDB ID: 6WZQ); and N5, a disordered domain. B) Sites of phosphorylation in the SR region of the N3 domain. Our experiments used two kinases – SRPK1 and GSK3β – resulting in a maximum of 10 phosphorylation sites. C) Hypothesized form and roles of N and phosphorylated N (pN). pN may have dynamic functions, forms liquid-like droplets with RNA and may localize to the surface of replication organelles. Unmodified N forms solid-like, spherical assemblies with genomic RNA and facilitates new virus encapsulation. N's form with RNA was characterized by Carlson et al., 2020, using light and

138 electron microscopy. D) A diagram of the SARS-CoV-2 lifecycle. Following viral entry (1), the
139 genome is uncoated (2) such that it can be read. Viral RNA is stored within viral replication
140 organelles (3) wherein RNA transcription and replication may be occurring. N binds to and
141 condenses genomic RNA exiting these organelles (4). In parallel, viral structural proteins are
142 produced (5), in preparation for viral encapsulation (6) and exit (7). E) Main RNA fragments used
143 in experiments are the first 1000 bases from the 5' end of the viral genome and the 1340 base
144 fragment encoding N. F) Droplets with varied morphologies form upon mixing 40 μM N (5% Alexa
145 Fluor 647 labeled) and 300 nM RNA fragments (5% Cy3 or Cy5 labeled) at 37˚C. Scale bar = 5
146 μm.
147

148 **N condensate composition determines interaction with membranes**

149 Prior work has shown that following viral infection, N accumulates in thin layers around
150 folded ER membranes that are likely vROs[40]. In contrast, later during viral budding events, N is
151 part of RNPs linked by the viral genome[25]. These RNPs do not fuse or grow during the budding
152 process, instead remaining as distinct complexes as the nucleocapsid is engulfed into new
153 virions[25,41]. We first asked whether we could reproduce these two behaviors of N in vitro.

154 We developed a system to study the interaction between N and RNA condensates and
155 membranes. We modeled membranes using giant unilamellar vesicles (GUVs). GUVs were made
156 with a lipid composition meant to approximate the human ER membrane[42,43], with 60% DOPC,
157 25% DOPE, 10% DOPS, and the addition of 5% Ni-NTA lipids. The Ni-NTA lipids allowed us to
158 tether membrane protein fragments to the GUV surface[44] to investigate whether the presence of
159 either of two viral membrane proteins would affect condensate-GUV interaction (Fig. 2A). The
160 viral non-structural protein 3 (Nsp3) localizes to vROs[45] and was suggested to both help form the
161 double layer of membranes as well as form pores that span the membranes[46–48]. Nsp3 is a known
162 interactor of N[49,50] and therefore is a logical candidate for modulating N's interaction with the
163 membranes enveloping vROs. We also studied the viral M protein that is present in the ERGIC

164 membrane where new virions form[51]. M and N are also known interactors, where M is thought to
165 anchor the RNP complex to the membrane during new virion formation[52,53]. Given the challenges
166 of producing and inserting transmembrane proteins into vesicles, we chose to study the domains
167 of the proteins that are known to interact with N. For M, we used a construct with the C-terminal
168 endodomain of the M protein, fused to a 6xHis tag and GFP[53]. For Nsp3, we took its ubiquitin-like
169 domain 1 (Ubl1)[49], and produced a construct with it fused to a 6xHis tag and GFP.

170 For this experiment, we used condensates composed of N or pN and the 1-1000 RNA
171 fragment. We added a small amount of GUVs and membrane protein fragments to the samples –
172 either Nsp3 or M fragments or a control solution (Fig. 2B). We observed the GFP signal from the
173 membrane proteins become localized to the surface of GUVs, with a similar degree of tethering
174 of Nsp3 and M fragments to the GUV surface (Supplementary Fig. 4). Next, we used optical
175 tweezers to control the position of condensates, moving them to and holding them at the GUV
176 surface. We then attempted to pull the condensates off the surface and observed whether they
177 remained bound or were mobile. For example, in a sample with pN, 1-1000 RNA, GUVs, and
178 Nsp3 fragments, we brought condensates composed of pN and 1-1000 RNA to the GUV and
179 observed as the condensates wet the surface (Fig. 2C).

180 We defined five types of interactions between condensates and membranes (Fig. 2D
181 legend): 1) With no interaction, the optical tweezer can move condensates away from a surface
182 it was in contact with. 2) With only binding, we observe the condensates remain attached to the
183 membrane surface even when the optical tweezer is attempting to dissociate the two, but no
184 additional condensate-membrane interactions occur. 3) During membrane wrapping, the
185 condensate binds to the membrane and the membrane surrounds the condensate over time. 4)
186 In partial wetting, the condensate not only binds to the membrane surface but also partially
187 deforms, expanding the area of contact between the condensate and membrane. 5) Finally, in
188 complete wetting, the condensates totally wet the membrane surface, forming a thin layer of
189 protein and RNA condensate.

190 We found that if no fragments of membrane proteins (Nsp3 or M) are present, no
191 interaction occurs between N and RNA condensates and the GUV surface, regardless of the
192 phosphorylation status of N (Fig. 2D and Movies S1-2). This suggests that N or pN and RNA
193 condensates have no intrinsic ability to interact with lipid membranes of the composition tested
194 (60% DOPC, 25% DOPE, 10% DOPS, 5% DGS-NTA(Ni), in 150 mM NaCl, 20 mM Tris-HCl, pH
195 7.5 buffer). In contrast, when the Nsp3 fragment is at the surface of GUVs, we observe
196 condensates composed of both N and pN binding to the membrane surface (Movies S3-4). With
197 unmodified N, condensates with 1-1000 RNA only partially wet the surface. Condensates with
198 phosphorylated N completely wet the surface, forming a thin layer of condensed material. This
199 behavior of pN and RNA condensates resembles the formation of a layer of protein on vROs that
200 is observed in infected cells[24]. Importantly, our results hint that by modulating the material
201 properties of N condensates, phosphorylation shifts the behavior observed from partial to
202 complete wetting. The thin layer of N that is observed surrounding vROs in infected cells may be
203 condensed pN wetting the surface due to pN-Nsp3 interactions.

204 When we repeated the experiment with the M fragment, we observed an important
205 difference in binding based on the status of N phosphorylation: while condensates with unmodified
206 N bound to the M-coated GUV surface, condensates with pN did not interact with the surface
207 (Movies S5-6). Therefore, phosphorylation of N may have unexpected effects beyond modulating
208 condensate material properties: it can act as a switch to prevent binding of pN to membrane
209 surfaces displaying the viral Membrane protein, where new virion formation typically occurs. (We
210 investigate how phosphorylation affects protein-protein interactions between N and M or Nsp3 in
211 Fig. 3). When condensates with N and 1-1000 RNA interacted with M-coated GUVs, we observed
212 binding (6/10 events) or membrane wrapping (4/10 events) (Fig. 2E), the difference between
213 either case likely driven by the membrane tension of the GUVs. In the cases where membrane
214 wrapping occurs, the protein and RNA condensates are partially engulfed into GUVs in the time
215 scale of minutes. The events of membrane wrapping are especially intriguing, given that they

216 resemble the direction of membrane bending required for encapsidation. These observations are
217 consistent with prior EM studies showing that RNPs may contribute to membrane bending after
218 recruitment to the membrane by M[54,55].

219 Given the important role that cholesterol plays in determining membrane fluidity, and
220 recent evidence pointing to its modulation of condensate-membrane interactions[56], we sought to
221 test the effect of adding cholesterol to our GUV membranes. Viral replication organelles originate
222 from ER membranes, which are known to be low in cholesterol content (~2 – 5%)[43]. Although the
223 SARS-CoV-2 virus buds from the nearby ERGIC[57], their membranes were found to include much
224 higher percentages of cholesterol (~25%)[58]. Therefore, we tested the effect of inclusion of 2, 5,
225 and 25% cholesterol on GUV membranes in place of DOPC (Supplementary Fig. 3). Addition of
226 cholesterol did not affect the binding interaction of condensates with membranes lacking viral
227 membrane fragments. Next, we observed that addition of cholesterol reduced the degree of
228 condensate wetting in cases where the GUV was coated with Nsp3 fragments, in a concentration-
229 dependent manner. However, as noted above, the ER-derived vRO membrane where N-Nsp3
230 interaction occurs is known to have low cholesterol content, and therefore we speculate that
231 cholesterol has a minor effect on N wetting to viral replication organelles. Finally, inclusion of
232 cholesterol did not affect the type of condensate-membrane interaction observed with M fragment
233 present. We conclude that although cholesterol can affect condensate-membrane interaction, in
234 the particular cases that are most physiologically relevant to SARS-CoV-2 infection, addition of
235 cholesterol did not change the interaction type we observed.

236 We quantified the affinity between condensates and GUVs by measuring the geometric
237 factor that considers the contact angles along the contact line between the GUV surface, the
238 condensate, and the external solution, as well as the intrinsic contact angle between condensate
239 and GUV (Fig. 2F-H)[39]. These are determined by the material properties of the condensate, the
240 strength of interaction between condensate and membrane surface, and the membrane tension
241 of the GUV. No interaction between condensates and the membrane results in the highest

geometric factors. An intermediate geometric factor is found with N condensates and Nsp3 fragments, where partial wetting is observed, and N condensates with M fragments, where either binding or membrane wrapping are observed. A drastic reduction in geometric factor occurs with pN and Nsp3, where complete wetting occurs. The different degrees of interaction also impact the intrinsic contact angle between condensate and GUV. Partial wetting or membrane wrapping cause an intermediate reduction in the angle, while complete wetting causes a drastic reduction in the angle (Fig. 2H). Overall, with this panel of condensate compositions and membrane surfaces, we were able to reproduce several behaviors that N displays during the viral lifecycle.

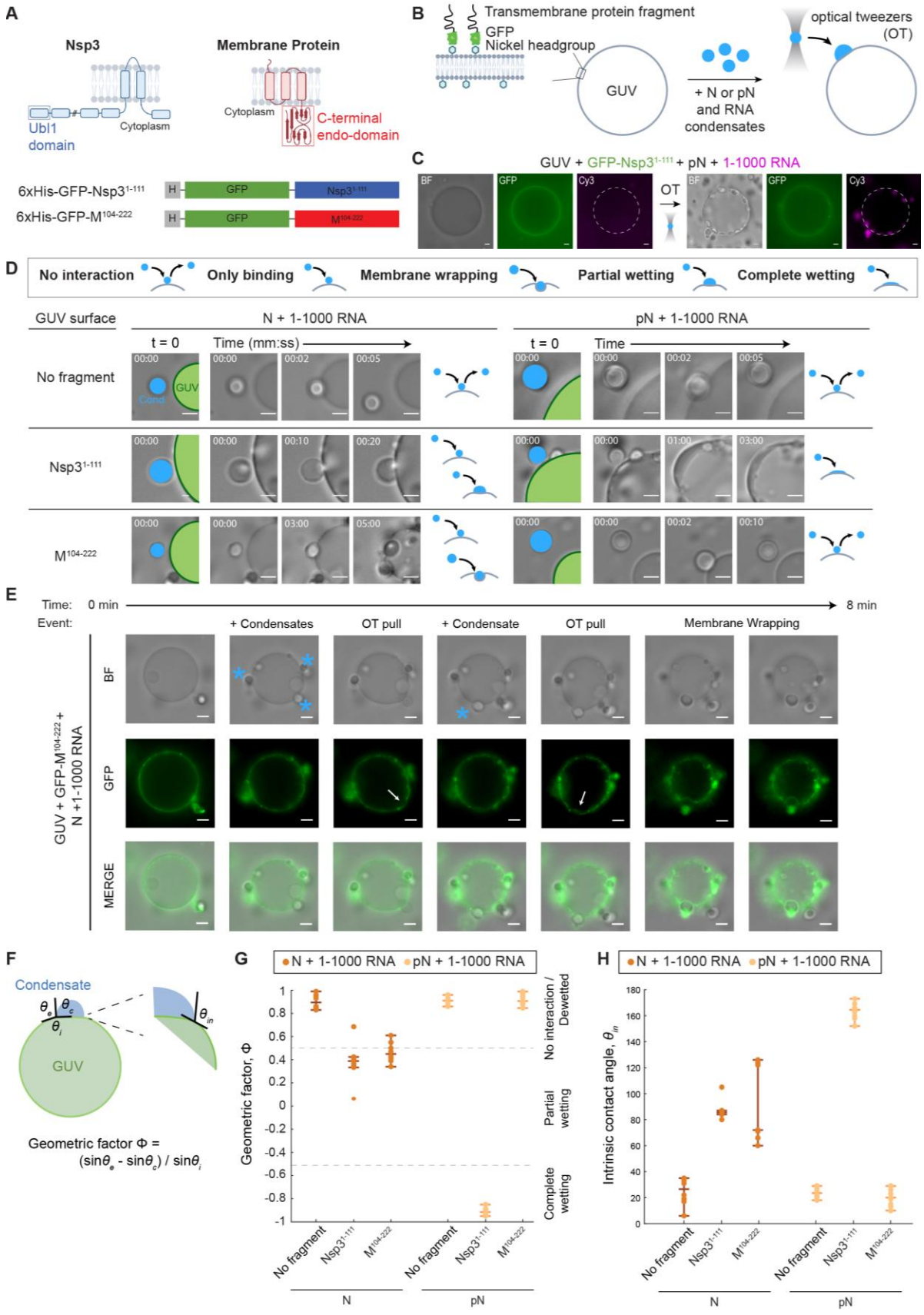
A
Nsp3
Membrane Protein
Ubl1 domain
Cytoplasm
Cytoplasm
C-terminal endo-domain
6xHis-GFP-Nsp3 1-111
6xHis-GFP-M 104-222
B
Transmembrane protein fragment
GFP
Nickel headgroup
GUV
+ N or pN and RNA condensates
optical tweezers (OT)
C
GUV + GFP-Nsp3 1-111 + pN + 1-1000 RNA
BF
GFP
Cy3
OT
D
No interaction
Only binding
Membrane wrapping
Partial wetting
Complete wetting
GUV surface
N + 1-1000 RNA
pN + 1-1000 RNA
t = 0
Time (mm:ss)
Time
No fragment
Nsp3 1-111
M 104-222
E
Time: 0 min
8 min
Event:
+ Condensates
OT pull
+ Condensate
OT pull
Membrane Wrapping
GUV + GFP-M 104-222 + N +1-1000 RNA
BF
GFP
MERGE
F
Condensate
GUV
Geometric factor Φ = (sinθe - sinθc) / sinθi
G
N + 1-1000 RNA
pN + 1-1000 RNA
Geometric factor, Φ
No interaction / Dewetted
Partial wetting
Complete wetting
No fragment
Nsp3 1-111
M 104-222
N
pN
H
N + 1-1000 RNA
pN + 1-1000 RNA
Intrinsic contact angle, θin

250

Figure 2: N condensate interaction with membranes. A) Fragments of the membrane proteins used to test membrane interactions: C-terminal endodomain of the Membrane (M) protein and the ubiquitin-like domain (Ubl1) of the Nsp3 protein. Both protein fragments are fused to a 6x Histidine tag and GFP. B) Schematic of the experimental setup showing the M or Nsp3 protein fragment tethered to the giant unilamellar vesicle (GUV) surface. Condensates composed of 40 μM N or pN plus 300 nM RNA are moved to the GUV surface using optical tweezers. C) Representative widefield images showing that Nsp3 fragments preferentially localize to the GUV surface (left) and condensates composed of pN and 1-1000 RNA wet the surface of GUVs after being delivered to the surface using optical tweezers (OT) (right). White dashed line added to denote the GUV surface. D) Representative widefield images showing the interaction between condensates and membranes over time, for N vs. pN, and comparing GUVs with no membrane protein, M fragment, and Nsp3 fragment. GUVs are labeled in green, and condensates (Cond.), in blue. Interaction type is qualitatively classified. E) Timelapse imaging showing several condensates (blue stars) being dragged by optical tweezers to the surface of a GUV, to which they bind. Optical tweezers can be used to pull bound condensates which results in deformation of the GUV surface (white arrows). Membrane wrapping occurs in one case. F) Sketch showing the parameters that define the geometric factor (Φ) and intrinsic contact angle (θ_{in}). Interaction leads to the formation of a contact line between the condensate interface and membrane. Contact angles $\theta_c + \theta_e + \theta_i = 360°$ and we can calculate Φ to describe the degree of wetting. Wetting can also be characterized by θ_{in} between condensate and membrane surfaces. G) Quantification of the geometric factor from each combination of condensate composition and membrane surface. Interactions that lead to membrane wrapping, partial wetting, or complete wetting result in reduced geometric factors. H) Intrinsic contact angle from each combination of condensate composition and membrane surface, calculated from the same image data set as G. n = 10 condensate-membrane interactions from n = 3 independent trials. Individual data points are shown for each

interaction event. The lines indicate the median, lower quartile, and upper quartile. Scale bars = 5 μm.

Phosphorylated N cannot bind to the SARS-CoV-2 Membrane protein

Given our observation that pN condensates did not bind to GUVs with M fragments, we examined whether phosphorylation affects protein-protein interactions between N and M or Nsp3. Several groups have sought to understand the binding mechanism between coronavirus N and M proteins[52,53], but no information is available on the effect of phosphorylation of N on its interaction with M. A stretch of amino acids (168–208) within the linker region of N was identified as critical for N-M interactions in the SARS-CoV-1 virus[52]. More recently, the linker domain of the SARS-CoV-2 N was shown to be necessary for N to co-phase separate with M[53]. Together, these studies point to a potential role of the SR-rich domain of N in interacting with M. Our results from Fig. 2 suggest that phosphorylation of the SR region of N may inhibit binding between N and M.

We performed a partitioning experiment using confocal microscopy (Fig. 3A). We added the fluorescently tagged M fragment or Nsp3 fragment to N or pN and observed the partitioning of the membrane protein fragments into condensates (Fig. 3B-C). We confirmed that M has a much stronger affinity to unmodified N than to pN. Unmodified N binds to M independent of the presence of viral RNA fragments, though phase separation is promoted by the presence of 1-1000 RNA. We observed contrasting results with phosphorylated N mixed with M. First, M does not drive the condensation of pN without addition of RNA. Second, M does not partition preferentially into condensates composed of pN and viral RNA (partition coefficient for M is 9.8 ± 0.3 in N + 1-1000 RNA condensates vs. 0.3 ± 0.1 in pN + 1-1000 RNA condensates; partition coefficient is defined as the ratio of average fluorescence intensity inside vs. outside the condensates). Given that M likely interacts with residues around N's SR domain[52], it is not surprising that phosphorylation of the SR region affects binding between the two proteins. These results are intriguing because they suggest a mechanism for timing of viral assembly. As noted

above, a majority of N within infected cells is phosphorylated, but N included within new virions is unmodified[16]. pN may not be incorporated into newly formed virions because this protein is unable to bind M and anchor the RNP to the membrane at the site of viral assembly.

As a comparison, we also investigated whether phosphorylation affects the partitioning of Nsp3 protein's Ubl1 domain into N or pN condensates. Previous reports showed that Nsp3 Ubl1 domain partitions into condensates composed of both N and a phosphomimetic version of N[19]. Our results qualitatively agree with these findings, although we found pN has a lower affinity than N for Nsp3, based on our measured partition coefficients (12.6 ± 0.1 for Nsp3 in N + 1-1000 RNA condensates vs. 2.2 ± 0.1 in pN + 1-1000 RNA condensates). Given the hypothesized role of N in delivering the viral genome to Nsp3-coated replication organelles following viral entry into cells, and given that the films of N observed adhered to replication organelles[24] are likely composed of phosphorylated N, it is not surprising that both unmodified and phosphorylated N bind to Nsp3.

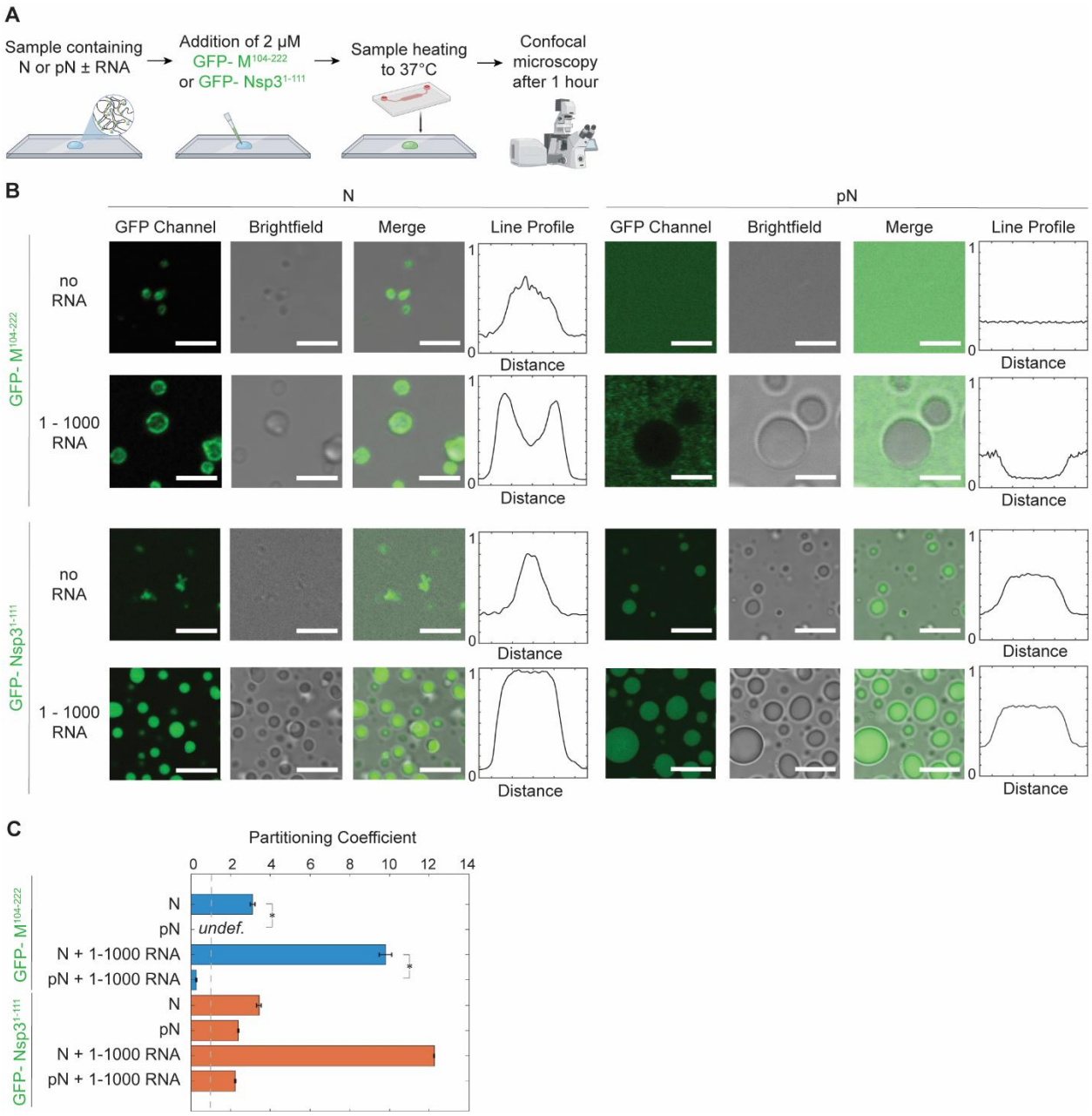

Figure 3: N and pN interaction with membrane proteins, M and Nsp3. A) Schematic of the experimental setup where 6xHis-GFP-M$^{104-222}$ or 6xHis-GFP-Nsp3$^{1-111}$ is added to a condensate sample and partitioning of GFP-tagged protein is quantified using confocal microscopy. B) Representative confocal images from condensates composed of 40 µM N or pN plus either no RNA or 300 nM RNA; plus either 2 µM 6xHis-GFP-M$^{104-222}$ or 6xHis-GFP-Nsp3$^{1-111}$. 6xHis-GFP-M$^{104-222}$ binds to N but not pN condensates while 6xHis-GFP-Nsp3$^{1-111}$ partitions in regardless of

choice of N vs. pN. Normalized line profiles across condensates, representing averages of at least n = 20 condensates from 3 independent trials. Scale bars = 5 μm. C) Quantification of partitioning of GFP-tagged proteins into N or pN condensates by dividing average fluorescence inside condensates by the average background fluorescence. Error bars represent one standard deviation (±1 s.d.). p values were determined using two-way ANOVA followed by post hoc Tukey's test. *$p < 0.01$.

Phosphorylation of N modulates the material properties of N condensates

Based on previous data on the liquid-like properties of pN condensates[19] and our membrane binding experiments, we hypothesized that the dynamic nature of pN condensates is what enables them to relax at the surface of GUVs. To explore the material properties of condensates, we first used Fluorescence Recovery after Photobleaching (FRAP). We photobleached either fluorescently labeled protein or RNA within a region of the condensate and observed how the fluorescence recovered over time. The advantage of using FRAP here is that it allows us to independently assess the dynamics of protein and RNA in our multi-component condensates. N bound to 1-1000 RNA recovers more slowly than pN bound to the same RNA (recovery half-life τ = 2.6 ± 0.1 min for N and 1.7 ± 0.1 min for pN) (Fig. 4A-B and Supplementary Fig. 5). This is in agreement with previous data showing a more rapid FRAP recovery in condensates with a phosphomimetic version of N compared to unphosphorylated N[19]. In addition, we also observe that the total recovery of N is lower compared to pN (62% vs. 94%), suggesting a pool of N is fixed to the RNA. Both metrics suggest that pN has a greater mobility than N when bound to 1-1000 RNA. In contrast to the results obtained by photobleaching protein within condensates, we observed almost no recovery of the fluorescence when RNA was bleached (Fig. 4A and C), independent of protein phosphorylation status. RNA appears to form a network onto which protein can bind and dissociate[59]. Individual RNA molecules may move locally but do not appear to diffuse long distances, likely due to their ability to form intermolecular base pairs.

347 Overall, our FRAP results support our hypothesis that differences in material properties contribute
348 in part to the type of condensate-membrane interaction observed. For example, condensates
349 composed of pN (which can wet surfaces) showed a greater protein recovery in FRAP
350 experiments, suggesting that the dynamic movement of pN allows the condensates to reorganize
351 at the surface of membranes over time.

352 To quantitatively assess how phosphorylation affects N condensate material properties,
353 we turned to passive microrheology. In passive microrheology, we embed 500 nm fluorescent
354 tracer beads into condensates and track their movement. The mean squared displacement (MSD)
355 of beads depends on their viscous and elastic environment[60]. Beads embedded within
356 condensates composed of pN + 1-1000 RNA displayed a greater MSD at all lag times when
357 compared to beads embedded in N + 1-1000 RNA condensates (Fig. 4D and Supplementary Fig.
358 6). The MSD of beads did not increase linearly with lag time for all samples, revealing that some
359 condensates behave as viscoelastic fluids under the experimental conditions. Using the
360 Generalized Stokes-Einstein Relation, we estimated viscous and elastic moduli. For N + 1-1000
361 RNA condensates, the elastic modulus dominates the viscous modulus at high frequencies (> 4
362 Hz). In contrast, for pN + 1-1000 RNA, the viscous modulus is dominant for all frequencies
363 measured (Fig. 4E – F). We then quantified the zero-shear viscosity of the samples, i.e., the
364 limiting value for viscosity at 0 Hz. For condensates composed of N + 1-1000 RNA, we found a
365 viscosity of 192 ± 3.6 Pa*s, while for condensates with pN, we measured a viscosity of 59 ± 3.4
366 Pa*s, representing a ~3x reduction in viscosity (Fig. 4G and Supplementary Fig. S7).

367 The change in viscosity upon phosphorylation of N may be due to modulation of protein-
368 protein and/or protein-RNA interactions, the latter via either specific or nonspecific binding to RNA.
369 We assessed each of these possibilities by testing the material properties of N or pN condensates
370 with unstructured RNA (polyrA) or with 5% PEG8000, which acts as a crowding agent to drive N
371 phase separation without RNA (Supplementary Fig. 2). Phosphorylation of N decreased the
372 viscosity of condensates with polyrA from 64 ± 4.2 Pa*s to 12 ± 0.4 Pa*s, suggesting that

373 nonspecific interactions between protein and RNA were disrupted. Furthermore, phosphorylation
374 decreased viscosity of condensates with PEG8000 from 11 ± 0.7 Pa*s to 4 ± 0.3 Pa*s, suggesting
375 that protein-protein interactions are also disrupted to some degree (Fig. 4G).

376 We also quantified the terminal relaxation time of the condensate network, which is the
377 inverse of the crossover frequency between the predominantly elastic and predominantly viscous
378 regimes. At timescales below the relaxation time, the condensates behave as elastic materials.
379 Elasticity is reduced by phosphorylation in both polyrA and 1-1000 RNA samples (Fig. 4H).
380 Condensates with N and polyrA or 1-1000 RNA have a relaxation time of 0.02 and 0.3 seconds,
381 respectively, while condensates with pN have no measurable relaxation timescale, suggesting
382 that phosphorylation disrupts the ability of N and RNA to crosslink (Supplementary Fig. 8). The
383 elasticity displayed by complexes formed between unmodified N and RNA may have a biological
384 function in protecting the RNA from mechanical stress[61].

385 We confirmed our material property measurements using micropipette aspiration
386 (MPA)[62,63]. We recorded how the length of the aspirated condensate in a micropipette changes
387 as a function of time in response to an applied pressure. We quantified the viscosity for the
388 different protein combinations and obtained the same trend and rank order that was observed
389 using microrheology (Fig. 4I and Supplementary Fig. 9). Viscosities quantified via MPA were
390 consistently lower than the zero-shear viscosities obtained from microrheology; when the two data
391 sets are plotted against each other, they have a linear fit with slope of 0.72 and R^2 of 0.99. Notably,
392 MPA measurements also showed that pN condensates have lower viscosity than the
393 corresponding N condensates. Together, our microrheology and micropipette aspiration results
394 point to N and RNA condensates being viscoelastic fluids whose properties depend on both RNA
395 type and phosphorylation status. Phosphorylation of N appears to loosen the network of
396 interactions between N and RNA, thus reducing the viscosity and elasticity of condensates.

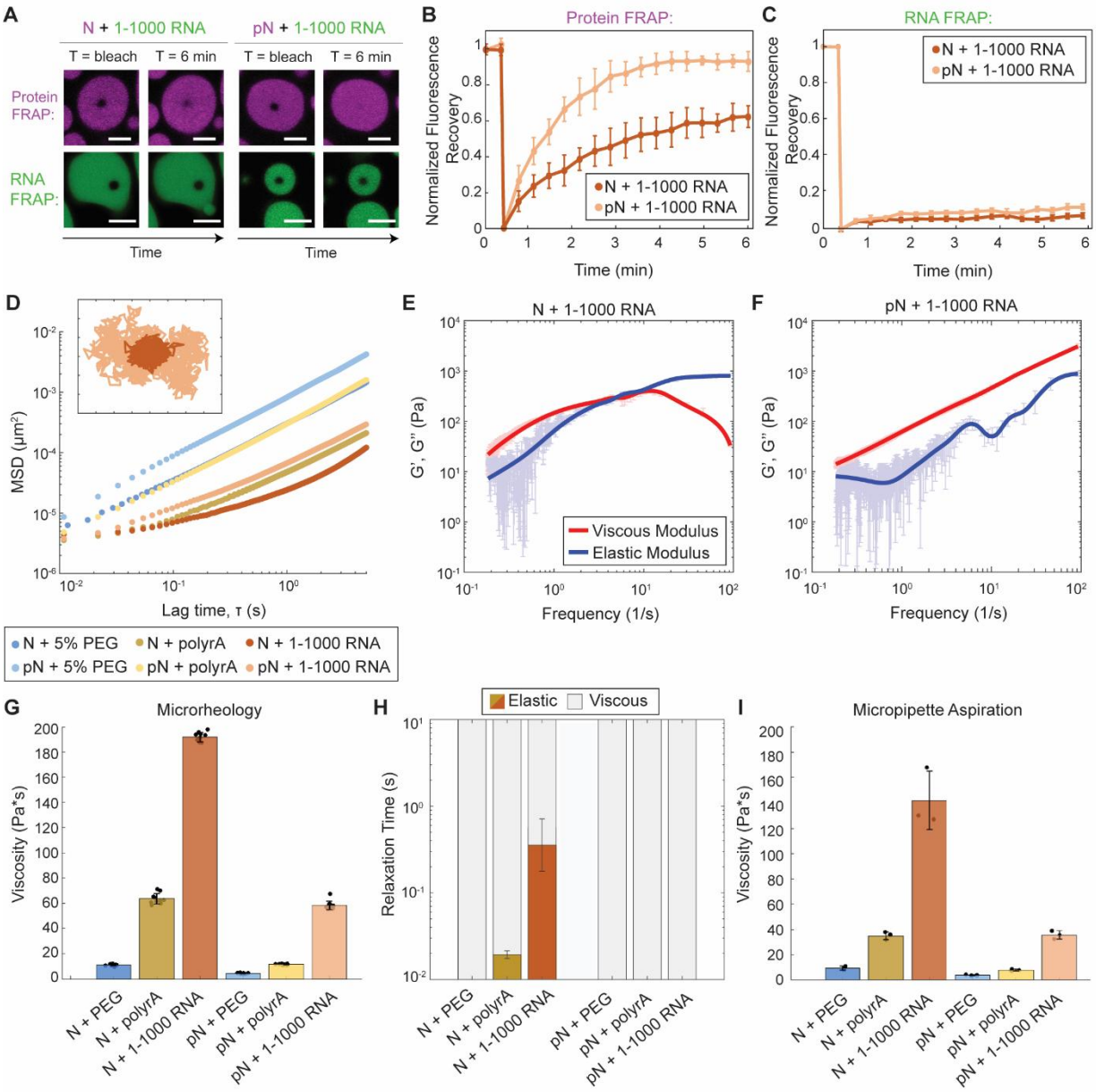

Figure 4: Phosphorylation modulates material properties of N and RNA condensates. A) Fluorescence recovery after photobleaching (FRAP) of N and RNA condensates, in which 5% of N/pN is labeled with Alexa-647 and 5% of RNA is labeled with Cy-3. pN recovers to a greater extent over time when compared to N, while in neither case does RNA signal recover. Scale bar = 5 μm. B) Quantification of FRAP of protein in N vs. pN condensates (n = 3 independent trials). C) Quantification of FRAP of RNA in N vs. pN condensates (n = 3 independent trials). D) Ensemble MSD versus lag time (prior to noise correction) for the protein and RNA combinations

tested in this study. Inset: Representative trajectories from two-dimensional particle tracking showing Brownian motion of beads in N vs. pN condensates with 1-1000 RNA. Each tick represents 5 nm. E) Plot with the average viscous modulus (G'', red) and the average elastic modulus (G', blue) of N + 1-1000 RNA condensates as calculated from the MSDs ($n \geq 10$ videos from 3 independent samples) after noise correction. F) The average viscous and elastic moduli after noise correction for pN + 1-1000 RNA condensates showing no crossover frequency in the range studied. G) The zero-shear viscosity of the protein and RNA condensates studied, calculated from the particle-tracking results after noise correction. Data from $n \geq 10$ videos from 3 independent trials. H) Quantification of the timescales at which the elastic modulus dominates (color) versus the viscous modulus dominates (grey) in protein and RNA condensates. I) Viscosity of the protein and RNA condensates from micropipette aspiration. $n = 3$ independent trials. Error bars represent one standard deviation (±1 s.d.).

RNA type also modulates condensate material properties

We repeated experiments with a second viral RNA fragment to assess whether our results depend on RNA sequence and structure. RNA sequence and structure are known to affect the material properties of other condensates, though most quantitative studies so far have focused on shorter, artificial RNA sequences[64,65]. For N protein, evidence exists that the morphology of condensates depends on the type of RNA included[66], however, the effect on condensate material properties has not been investigated. Here, we compare our results with 1-1000 RNA with N RNA, introduced previously, which encodes the N protein and is 1340 base pairs long. N RNA is an important viral RNA to test because it is abundant in infected cells, and from a biophysical perspective, it is (1) longer than 1-1000 RNA, and as such has a higher ensemble diversity (which describes the diversity of conformations the RNA is predicted to fold into; it is predicted to be 198.5 for N RNA vs. 148.1 for 1-1000 RNA, based on ViennaRNA[67]), and (2) contains a different pattern of preferred binding sites for N[66]. These factors suggest that N RNA forms a more entangled

431 network in condensates compared to 1-1000 RNA, resulting in the different condensate
432 morphologies observed (Fig. 1F). We found similar behavior between condensates with 1-1000
433 or N RNA (Supplementary Fig. 10), both in terms of binding to GUVs with different membrane
434 protein fragments, as well as their material response to phosphorylation (phosphorylation reduces
435 viscosity and elasticity). These results suggest that the change in N condensate material
436 properties and membrane interaction upon phosphorylation are not RNA structure dependent.
437 Across experiments, we did observe that condensates with the longer N RNA were less likely to
438 deform than their counterparts with 1-1000 RNA. This data hints that complexes of unmodified N
439 and longer fragments of RNA, such as genomic RNA, would appear solid-like and with an
440 important elastic response, which may play a role in mechanically protecting RNA within virions[61].
441 To further study these questions, additional analyses with varying RNA lengths and structures
442 would be required.
443

444 **Phosphorylation weakens binding between N and RNA by promoting intra-dimer**
445 **interactions**

446 We have shown that phosphorylation of N results in condensates that more readily deform
447 at membrane surfaces and that have lower viscosity and elasticity, both likely driven by a
448 loosening of the interaction network between protein and RNA. This change in interaction does
449 not appear to be dependent on specific RNA structures, as phosphorylation also drastically
450 softens condensates with unstructured polyrA (Fig. 4G-I). We therefore asked how
451 phosphorylation affects N, such that interaction between protein and RNA is diminished.

452 We leveraged fluorescence polarization to measure the binding affinity between N protein
453 and fluorescently labelled RNA (Fig. 5A-B). First, we assessed whether phosphorylation affects
454 binding of N to a stem-loop structure (SL4) present in the 1-1000 RNA fragment. SL4 was
455 identified as a preferred binding site for N's RNA binding domain[30,31]. Phosphorylation of N
456 reduces the binding affinity to SL4 RNA, increasing the dissociation constant (K_D) from 10.9 ± 1.4

nM to 59.0 ± 0.9 nM. Although this is a six-fold reduction in binding affinity, the concentrations at which our membrane interaction and material property experiments were conducted are well above the nanomolar K_Ds measured, and therefore this change in binding cannot explain the material property changes observed. Next, to test the hypothesis that nonspecific binding between protein and RNA is disrupted by phosphorylation, we measured the binding affinity between N or pN and a 30-base polyrA. Phosphorylation causes a twenty-fold change in K_D from 71.7 ± 0.8 nM to 1571.0 ± 2.1 nM, larger than that observed for the SL4 RNA. We conclude that phosphorylation reduces N's interaction with unstructured RNA more so than structured RNA. Importantly, for both polyrA and SL4, phosphorylation of N also reduced the maximum polarization. This suggests a greater rotational freedom in the protein-RNA complexes formed with pN that could be driven either by the formation of a more compact complex or a conformation in which the protein-bound RNA retains more rotational mobility[68]. We anticipated that phosphorylation would weaken binding between N and RNA due to electrostatic repulsion. However, our fluorescence polarization results suggest that phosphorylation may also be inducing a conformational change in N that affects its RNA binding properties.

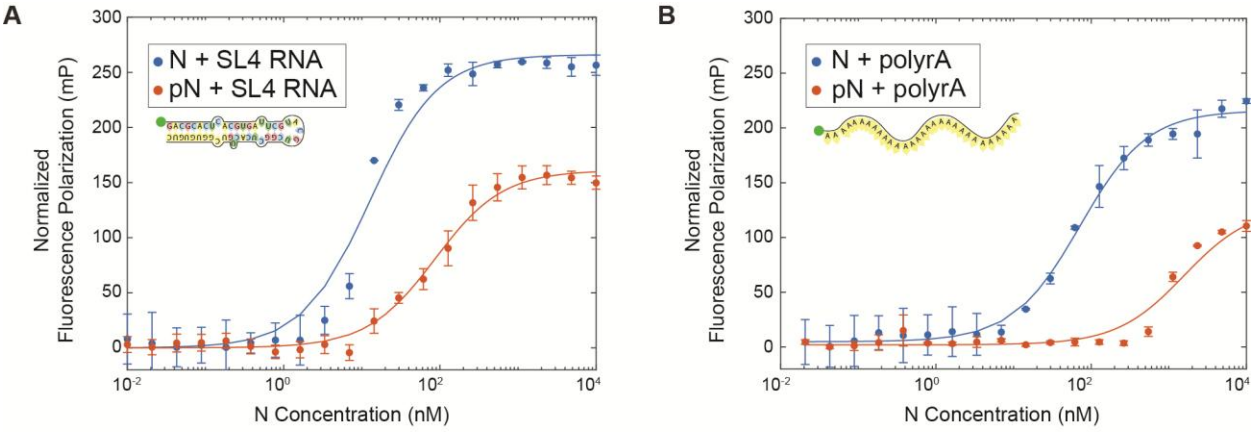

Protein + RNA	K_D (nM)	Δ Polarization (mP)
N + SL4 RNA	10.9 ± 1.4	252.2 ± 6.2
pN + SL4 RNA	59.0 ± 0.9	152.6 ± 3.5

Protein + RNA	K_D (nM)	Δ Polarization (mP)
N + polyrA	71.7 ± 0.8	217.1 ± 5.8
pN + polyrA	1571.0 ± 2.1	106.2 ± 2.3

Figure 5: N protein phosphorylation weakens RNA binding affinity. A) Quantification of binding affinity between N vs. pN and the viral stem loop 4 RNA (SL4) based on a change in

475 normalized fluorescence polarization (minimum polarization set to 0). n = 3 independent trials. B)
476 Quantification of binding affinity between N vs. pN and unstructured 30 base polyrA from
477 normalized fluorescence polarization. n = 3 independent trials.
478
479 To assess the conformational change of the N protein dimer following phosphorylation, we
480 used Small Angle X-ray Scattering (SAXS), a technique compatible with the size and largely
481 disordered nature of N protein. Our SAXS results indeed show that N and pN are partially
482 disordered dimers in solution. This is in agreement with previously published data on unmodified
483 N protein;[9] SAXS of pN had not been previously reported. With phosphorylation, we found a
484 significant decrease in radius of gyration (R_g), from 60.2 ± 1.3 Å for N to 54.4 ± 2.0 Å for pN, a
485 finding supported by both the pair distance distribution and the Guinier approximation (the
486 decrease in R_g was consistent across concentrations) (Fig. 6A-B and Supplementary Fig. 11-12).
487 The shape of the pair distance distribution function also changes with phosphorylation. The
488 presence of multiple peaks in the unmodified N data highlights the multi-domain nature of the N
489 protein dimer[69]. The lack of these peaks in the phosphorylated N data suggests the domains can
490 no longer be resolved, indicating there may be new interactions bringing the different parts of the
491 protein together. Next, analyzing normalized Kratky plots confirms both N and pN display behavior
492 typical of a multidomain protein with flexible linkers (Fig. 6C)[70]. The elevated tail for N indicates
493 greater extension of the protein compared to pN. Using the scattering data to construct bead
494 models for N and pN allows us to visualize these changes (Fig. 6D-E and Supplementary Fig.
495 13). Our bead models show a new region of electron density between monomers within pN
496 dimers, suggesting that indeed new interactions within pN dimers take place that are not present
497 in N dimers.
498 To better understand how the conformation of N changes upon phosphorylation, we used
499 single-molecule Förster Resonance Energy Transfer (smFRET). First, for full-length N, we
500 confirmed that phosphorylation does not affect the conformation of the dimerization domain[71] or

501 the tendency of N to dimerize (Supplementary Fig. 14). Next, we used smFRET to study the
502 conformation of the linker region. We probed two constructs of N with fluorescent labels flanking
503 the linker region (at residues 172 and 245): full-length N and truncated N^{1-246}, which lacks the
504 dimerization and C-terminal disordered domains. We performed experiments at two protein
505 concentrations: low concentration (100 pM labeled protein), at which N is in its monomeric form,
506 and high concentration (100 pM labeled protein + 1 μM unlabeled protein for full-length N or 4 μM
507 unlabeled protein for N^{1-246}), at which dimers form if the dimerization domain is present. We
508 measured the distribution of transfer efficiencies for each protein construct at each concentration
509 (Supplementary Fig. 15). The distributions represent a dynamic ensemble of conformations, as
510 supported by the corresponding analysis of donor lifetime vs. transfer efficiency (Supplementary
511 Fig. 15). Therefore, we used the mean transfer efficiencies to calculate the root mean square
512 distance (RMSD) between labelled residues, which can be compared across samples to
513 understand the degree of expansion of the linker (Supplementary Fig. 15). Consistent with
514 previous measurements of the same constructs[8], we observed a mean transfer efficiency across
515 the linker of approximately 0.6 for full-length N and 0.75 for N^{1-246}. We found that phosphorylation
516 causes an expansion of the linker region, which was unexpected given that we previously
517 measured by SAXS a reduction in radius of gyration of the N dimer with phosphorylation.
518 However, analysis of the sequence charge decoration (SCD) of the linker supports our smFRET
519 findings and suggests that addition of several negative charges to the domain causes local
520 repulsion that results in expansion[72] (Supplementary Fig. 15). Importantly, our smFRET results
521 show that the degree of expansion due to phosphorylation is greatly reduced in the full-length
522 construct under dimer conditions. To reconcile the SAXS and smFRET results, one possibility is
523 that phosphorylation of the N dimer drives formation of new interactions across linker domains of
524 the dimer that counteract the expansion caused by phosphorylation.

525 To explore the new interactions that arise upon N protein phosphorylation, we conducted
526 coarse-grained molecular simulations of the protein. We combined the HPS-Urry model for

527 simulation of disordered proteins[73,74] with an elastic network model and Center of Mass (COM)
528 bead placement scheme for modeling folded domains[75]. To mimic the effects of phosphorylation,
529 we used phosphomimetic mutations (S to D and T to E). We found reasonable agreement
530 between the radii of gyration measured in SAXS and those predicted in the simulations, which
531 were 55.5 Å for N and 52.4 Å for phosphomimetic N (SAXS results were 60.2 ± 1.3 Å for N to 54.4
532 ± 2.0 Å for pN). Fig. 6F depicts three conformations of N protein that were captured by the
533 simulation, with a range of radii of gyration. Next, we compared the pair distance distributions
534 from our simulations of N and phosphomimetic N protein with SAXS data (Fig. 6G-H). Although
535 the simulation captured the overall collapse of N upon phosphorylation, it did not fully capture the
536 change in conformation of the protein that we observed through SAXS, which is reflected in the
537 shape of the pair distance distribution function[69]. This indicates that while the simulation model
538 may capture accurate conformations, it lacks the level of detail needed to consistently match
539 experimental data across the full ensemble.

540 To refine our simulation, we incorporated information from our SAXS experiments. We
541 used a Bayesian Maximum Entropy ensemble reweighting scheme to adjust the statistical weights
542 of the simulated conformations so that their pair distance distribution better matches the
543 experimental SAXS data[76] (Supplementary Fig. 16). This helps identify subsets of conformations
544 that explain the experimental data, which may have been undersampled due to shortcomings in
545 the simulation or missing environmental effects. For example, the phosphomimetic mutations
546 used in simulations lack the additional steric bulk of phosphate groups and simulations may not
547 fully capture how the ionic conditions in experiments modulate electrostatic interactions involving
548 the phosphate groups[77]. Upon reweighting, the radii of gyration obtained for N and
549 phosphomimetic N more closely matched the values obtained from SAXS, with 58.5 Å for N and
550 55.0 Å for phosphomimetic N (Supplementary Fig. 17A-B). The pair distance distribution function
551 from the reweighted simulation also more closely resembled the data obtained from SAXS (Fig.
552 6F-G). For example, with reweighting, the discrepancy between the pair distance distribution for

553 N reduces from a χ^2 of 7.5 to 2.2. Finally, with reweighting, we also observe agreement between
554 simulations and smFRET results regarding the expansion of the linker domain (Supplementary
555 Fig. 17).

556 We then investigated the change in intra- and inter-domain interactions predicted by the
557 simulation with phosphomimetic mutations (Fig. 6I-J). With the simulation, we can quantify the
558 change in number of contacts between residues both within each monomer and across monomers
559 in a dimer. We found that most intramonomer interactions decrease in the phosphomimetic protein
560 compared to unmodified N, with the exception of N2-N2 and N3-N4 interactions. While the N2
561 domain was almost entirely held folded by the harmonic constraints of the simulation, the last 13
562 residues of the domain were left flexible due to their high b-factor in the reference crystal structure.
563 Following the phosphomimetic mutations to the nearby linker (N3), these 13 residues interact with
564 the folded part of the N2 domain at a higher frequency (Supplementary Fig. 18A). Separately, the
565 increase in N3-N4 interactions observed is likely driven by the negative charges added to the N3
566 domain interacting with a positive patch of residues in the beginning of the N4 folded domain
567 (Supplementary Fig. 18B). Interestingly, we observe a significant decrease in intramonomer
568 interaction within the N3 domain, which matches our smFRET observations. The main driver of
569 this loss of interaction is a decrease in contact between nearby residues of the SR-rich region
570 following the addition of several negative charges due to the phosphomimetic mutations
571 (Supplementary Fig. 18C). In terms of intermonomer interactions, we found a gain in interaction
572 for almost all combinations of domains of N. In particular, we observe that the linker (N3) gains
573 contacts with the other monomer's N2, N3, and N4 domains. The N3 domain gains interactions
574 with an arginine-rich patch on the N2 domain and it interacts directly with the SR-rich region of
575 the opposite N3 domain, which is likely also driven by interactions with arginine residues
576 (Supplementary Fig. 18D-E). Finally, the N3 domains interacts with a positively charged patch in
577 the N4 domain, which is rich in both arginine and lysine residues (Supplementary Fig. 18F).
578 Therefore, binding between the negatively charged phosphomimetic residues and positively

579 charged arginine and lysine residues are the main source of new interactions within the
580 phosphomimetic N dimers.

581 Together, our SAXS, smFRET, and simulation results support that a conformational
582 change in N occurs as a result of phosphorylation. Previous molecular simulation of a fragment
583 of N containing the linker domain (N3) had found a phosphorylation-induced increase in intra- and
584 inter-molecular contacts due to the formation of salt bridges between phosphate groups and
585 arginine side chains[26]. Our results partly agree with these findings: while intramonomer N3
586 interactions decrease, binding between arginine residues and phosphate groups across members
587 of a pN dimer appears to be the basis for the new inter-monomer interactions observed. Overall,
588 we speculate that new interactions within and between monomers occupy the linker and thus
589 interfere with N's ability to bind to RNA. The more compact conformation of pN dimers and
590 reduced affinity between protein and RNA[10] explain our earlier observations from the binding
591 affinity assay and material property measurements. Therefore, this new model ties together the
592 conformational change of N upon phosphorylation with its reduced ability to interact with RNA,
593 which in turn affects its condensate material properties and its form when interacting with
594 membranes.

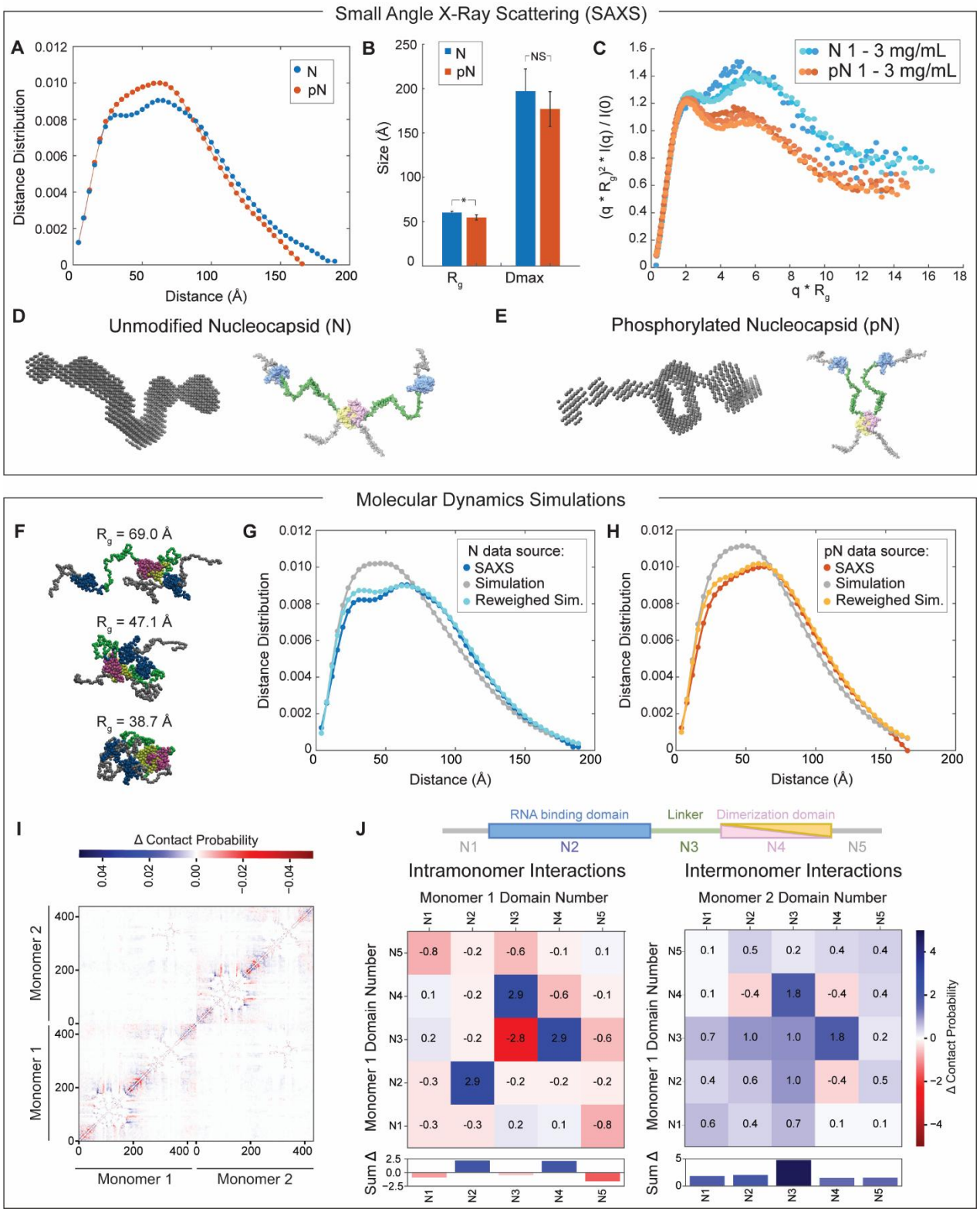

Figure 6: N protein phosphorylation weakens RNA binding affinity due to change in protein conformation. A) Representative pairwise interatomic distance distribution P(r) derived from

598 SAXS for N and pN. N or pN concentration = 3 mg/mL. B) The maximum dimension (D_{max}) and
599 radius of gyration (R_g) for N and pN derived from the pair distance distributions. Error bars
600 represent one standard deviation (±1 s.d.). p values were determined using two-sided student's
601 t-test; asterisk indicates $p < 0.05$. C) Normalized Kratky plot comparing the scattering of N vs. pN,
602 indicating a structural change has occurred due to phosphorylation. Concentrations shown for N
603 or pN are 1, 1.5, and 3 mg/mL from lighter to darker. D) Bead model representation for the N
604 dimer developed from SAXS results (left) and hypothesized conformation of N (right). E) Bead
605 model representation for the pN dimer developed from SAXS results (left) and hypothesized
606 conformation of pN highlighting new intermolecular interactions (right). F) Snapshots from N
607 simulation depicting conformations that demonstrate the protein's representative collapsed and
608 extended states. The radius of gyration of each selected conformation is noted. G) Comparison
609 of the pairwise interatomic distance distribution P(r) derived from SAXS and molecular dynamics
610 simulation before and after reweighting with SAXS data for N. H) Comparison of the pairwise
611 interatomic distance distribution P(r) derived from SAXS and molecular dynamics simulation
612 before and after reweighting with SAXS data for pN. I) Change in contact probability between all
613 residues within a dimer, compared between N and phosphomimetic N simulations. Lower left and
614 upper right quadrants represent intramonomer interactions while the upper left and lower right
615 quadrants represent intermonomer interactions. Blue coloring indicates more frequent
616 interactions occurred in phosphomimetic N compared to unmodified. J) Analysis of the difference
617 in intra-monomer (left) and inter-monomer (right) interactions between N and phosphomimetic N,
618 per domain of the protein (as defined by the schematic of N above). Positive numbers / blue
619 coloring indicates more frequent interactions occurred in phosphomimetic N compared to
620 unmodified. Below, sum of change in interactions across each domain for both intra- and inter-
621 domain interactions.
622

Discussion

Despite significant interest, there is still limited knowledge about how the SARS-CoV-2 N protein is regulated during viral replication. Our work was motivated by three open questions. First, N is thought to have several functions during viral replication, including regulating viral RNA transcription and translation, and facilitating encapsulation of genomic RNA[2,3]. How can one protein perform such distinct functions? Second, N's regulatory functions likely occur near viral replication organelles[40], while its role in RNA encapsulation is known to take place at the surface of the ERGIC membrane, where viral budding occurs[25]. How does N associate with these different membranes? Third, N is known to phase separate in vitro and when expressed in cells[3,30,53]. However, is phase separation important for the function of N during viral replication? Building upon prior research, we reasoned that phosphorylation holds a clue to answering these three questions. Phosphorylation was previously hypothesized to be the key mechanism of regulation of N during viral replication[19]. Two populations of N exist inside infected cells, with the majority of N being phosphorylated, but with N that is incorporated into new virions remaining unmodified[13–17]. Phosphorylation was also shown to alter the behavior of N condensates[19]. We combined these observations to formulate a new hypothesis: that phosphorylation may be responsible for toggling N between its functions by modulating the material properties of N condensates and thus switching between its two membrane-associated states.

In this work, we reveal membrane association as a key feature of N phase separation. We argue that the phosphorylation state of N determines its two membrane-associated behaviors in infected cells: 1) being adhered to membrane surfaces and 2) being tightly bound to RNA when engulfed into new virions. Our experiments show that phosphorylation modulates the material properties of N and RNA condensates, and thus the type of interaction between condensates and membranes, which is important for the function of N. We next studied N at a molecular level and identified that phosphorylation results in new interactions within and between the monomers of a dimer, thus interfering with the protein's ability to interact with RNA. We propose a model that ties

649 together an understanding of how phosphorylation acts as a switch controlling the conformation
650 of N and its behavior during viral replication (Fig. 7). In its phosphorylated form, N prefers
651 intermolecular interactions between N monomers within a dimer over interaction with RNA, thus
652 resulting in a looser network formation, condensates that can remodel at the membrane surface,
653 and RNA that is more accessible during replication steps. In its unmodified form, N binds tightly
654 to RNA, and facilitates its encapsulation after being anchored to the membrane surface by N-M
655 interactions. Through this model, we suggest that phase separation is critical to SARS-CoV-2
656 replication and that phosphorylation is a key mechanism through which phase separation is
657 regulated to allow N to complete its functions at membrane surfaces.

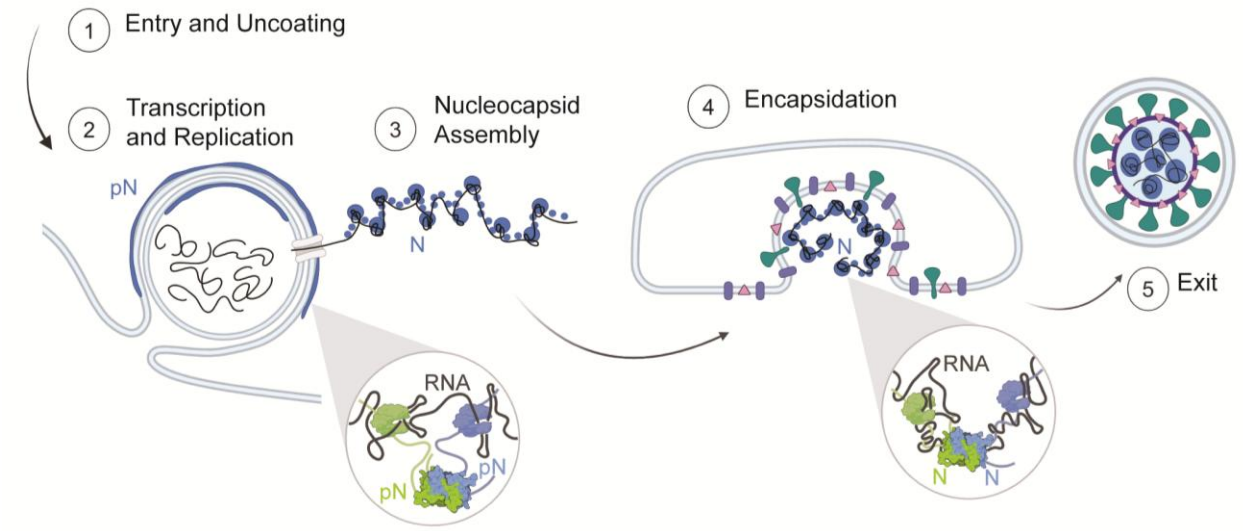

658

659 **Figure 7: Model of N protein form and membrane-associated state during the viral lifecycle.**
660 Inside the cell (1), the vast majority of N is found in its phosphorylated form, localized to the
661 surface of viral replication organelles (2). Phosphorylation promotes linker-linker interactions
662 across N dimers that weaken interaction between N and RNA (inset, left). This looser protein-RNA
663 interaction network within condensates results in a relatively low viscosity and elasticity that may
664 facilitate the molecular diffusion needed during RNA transcription and replication. A second
665 population of N that is destined to form new virions binds to new viral genomic RNA (gRNA) and
666 condenses RNA into small spherical complexes (3). This unmodified protein binds tightly to gRNA

667 through both specific and nonspecific interactions (inset, right). These assemblies have high
668 viscosity and elasticity that may support a protective function of N towards gRNA. The gRNA and
669 N capsid is engulfed by the ERGIC membrane, facilitated by N and M interactions (4). New virions
670 exit the infected cells (5).
671
672 Our results are distinct from recently published data on the effect of phosphorylation on
673 the molecular conformation of N determined using NMR. Botova et al. found a rigidification of the
674 SR region upon phosphorylation that their data suggests is a result of new interactions with the
675 RNA binding domain[78]. Their conclusions are due to the similarity in the chemical shift
676 perturbations observed when N is phosphorylated vs. when RNA binding occurs. However, the
677 rigidification of the SR region could also be due to the presence of bulky phosphate groups.
678 Though new interactions between N's RNA binding domain and the linker region could be
679 overlooked by our SAXS-derived reconstruction given its low resolution, our results point to a
680 larger conformational shift of the dimer. Stuwe et al. also studied the effect of phosphorylation on
681 N using NMR, though the construct studied lacked the N-terminal RNA binding domain, thus
682 potentially skewing the analysis of intra- and inter- molecular interactions[79]. They found that
683 phosphorylation changes the behavior of a leucine-rich helix (LRH) found in N's linker: in
684 unmodified N, higher order oligomers form through LRH self-interaction that is significantly
685 weakened by phosphorylation. In contrast with these results, our data presents an alternative
686 model in which phosphorylation of N promotes intermolecular interactions between the SR
687 regions of monomers within a dimer and thus disrupts non-specific interaction between pN and
688 unstructured RNA. We do not observe a significant change in the oligomerization behavior of N
689 following phosphorylation (Supplementary Fig. 14).
690 Our findings suggest several pathways towards development of novel COVID
691 therapeutics. One is to target the relevant kinases. A recent study suggested that N in cells is
692 sequentially phosphorylated by host kinases SRPK1, GSK-3, and CK1[17]. Indeed, inhibiting

693 SRPK1 was found to reduce viral replication, while blocking GSK-3 activity decreased replication
694 in cells and reduced infection in patients[17,80]. Second, our results suggest that a population of
695 unmodified N protein is necessary for viral encapsulation and formation of new virions. Although
696 the source of this population of unmodified N is less understood, a phosphatase was identified to
697 act on the murine coronavirus N protein[81]. Similar phosphatases should be identified for the
698 SARS-CoV-2 N protein and explored as treatment targets. Third, our results also highlight that
699 phase separation may be critical for the functions of N protein, and particularly that the material
700 properties of condensates can support N's functions. Therefore, condensate-modifying
701 molecules, which may not directly interact with N but do partition into condensates and affect their
702 properties, may also interrupt viral replication and should explored as treatments. Fourth, an
703 alternative approach to inhibiting viral replication is to target RNA structure. We identified that
704 RNA structure is important in determining the material properties of N and RNA condensates, and
705 as such, molecules that disrupt viral RNA structure may be potential treatments for viral infection.
706 For example, Vögele et al. identified a molecule that disrupts the double-stranded structure of
707 stem loop 4 (SL4) in viral RNA[82]. Further investigation is needed to assess whether this type of
708 disruption modulates the material properties of N and RNA condensates in a manner and extent
709 that impairs N's functions in viral replication.

710 Although significant progress has been made in understanding the mechanisms of SARS-
711 CoV-2 replication in infected cells, here we turned to an in vitro system to investigate the
712 biophysical mechanisms driving the behaviors observed in cells. Where possible, we opted to
713 include components in our system that mimic physiological conditions, such as in vitro
714 phosphorylated N instead of a phosphomimetic version, and fragments of viral RNA instead of
715 unstructured RNA. Using an in vitro system has allowed us to investigate mechanisms that would
716 be challenging to measure in cells, such as quantifying how specific membrane protein domains
717 affect condensate-membrane interactions, how specific RNA structures affect strength of N
718 protein binding, and how phosphorylation affects the conformation of N protein. However, we

719 recognize that within the crowded environment of the cell, and with many other interaction
720 partners present during viral infection, the behaviors of N may be different than those we studied
721 in vitro. For example, phosphorylation of N protein has been shown to promote its interaction with
722 14-3-3 proteins, which are abundant in cells[83,84]. In our system, we did not consider how binding
723 to 14-3-3 proteins may change how pN interacts with other viral membrane proteins and
724 membranes. Therefore, further studies in infected cell models are necessary to verify our findings.
725 For example, in Scherer et al., the location of pN was identified as the surface of replication
726 organelles by studying infected cells that were fixed and stained. This experiment should be
727 repeated with cells that are treated with SRPK1/2 inhibitors to verify how inhibition of
728 phosphorylation affects the localization of N.

729 In conclusion, we have investigated the connection between N protein's molecular
730 conformation, its material properties when phase separated with RNA, and its membrane-
731 associated behavior. We show that phosphorylation may act as a switch to toggle N between its
732 two membrane-associated states during viral replication. Given the complexity of the system
733 studied, further investigations are needed to better understand how our results apply to other N
734 protein interactions that occur in infected cells. This includes considering factors such as the
735 complex composition of lipid membranes, as well as the presence of both human mRNA and the
736 much longer viral genomic RNA.

737

738 **Acknowledgements**

739 We thank Christine Roden and Amy Gladfelter for helpful discussion, for sharing plasmids
740 for making RNA fragments and fluorescently labeled viral RNA; Mihai Solotchi and Smita Patel
741 for assistance with fluorescence polarization experiments and helpful discussions; Gabriela
742 Tirado-Mansilla for assistance preparing SAXS samples; Bineet Sharma for help with GUV
743 production; Srinivas Chakravartula and Haiyan Zheng for assistance with mass spectrometry;
744 Kevin Corbett and Qiaozhen Ye for sharing the GFP-Mfragment plasmid; and Jean Baum and

Vikas Nanda for helpful discussion. This work was supported by NIH grants R35GM142903 (to B.S.), R35GM147027 (to Z.S), R35GM138296 (to A.G.), R35GM150589 (to G.D.) and National Science Foundation grant DMREF-2118860 (to S.M. and A.G.). X-ray scattering measurements were done at the NSLS-II beamline 16-ID (LiX) at Brookhaven National Laboratory. The LiX beamline is supported by an NIGMS P30 Grant (P30GM133893), NIH Grant S10 OD012331, the DOE Office of Biological and Environmental Research (KP1605010), and the DOE Office of Science, Office of Basic Energy Sciences Program under contract number DE-SC0012704 to CBMS. Figure 1C-D: Created in BioRender. Favetta, B. (2024) BioRender.com/o21g999. Figure 2A-B: BioRender.com/s97t568. Figure 7: Created in BioRender. Favetta, B. (2022) BioRender.com/382j936.

Author Contributions

BF: conceptualization, experimental design, data collection and analysis, writing—original draft, writing—review and editing; HW: data collection for MPA experiments; JC and AS: experimental design, data collection and analysis for smFRET experiments; AS: data collection for simulations; MB: data analysis for microrheology experiments; CR: data collection and analysis for SAXS experiments; GD: experimental design, data collection and analysis for simulations; SM: experimental design, data collection, analysis and supervision for SAXS experiments; AJG: supervision of SAXS data analysis and funding acquisition; ZS: supervision, experimental design for MPA and GUV experiments and funding acquisition; BSS: conceptualization, supervision, experimental design, data analysis, writing—original draft, writing—review and editing, funding acquisition.

Declaration of Interests

The authors declare no competing interests.

771 **Resource Availability**

772 **Lead contact:** Requests for further information and resources should be directed to and will be
773 fulfilled by the lead contact, Benjamin S Schuster (benjamin.schuster@rutgers.edu).

774 **Materials availability:** Plasmids generated in this study will be deposited to Addgene (links will
775 be made available upon publication).

776 **Data and code availability**: All the quantitative analyses discussed in this paper were generated
777 based on data and computer codes that will be made publicly available (links will be made
778 available upon publication).

779

780 **Supporting information**

781 SI Appendix: Table S1, Supplementary Fig. 1–18, SI References
782 Movies S1-6, related to Figure 2.

783

784 **Materials and methods**

785 **Cloning**

786 All genes of interest were cloned into pET vectors in frame with N-terminal 6x-His tags. A
787 TEV protease site was inserted between the 6x-His tag and the Nucleocapsid protein coding
788 sequence. Constructs were cloned by DNA assembly (NEBuilder HiFi DNA Assembly Master Mix;
789 New England Biolabs). Gene sequences were verified by Sanger sequencing (Genewiz).

790 **Protein expression and purification**

791 For bacterial expression, plasmids were transformed into BL21(DE3) competent E. coli
792 (New England BioLabs). Colonies picked from fresh plates were grown for 12 hours at 37 °C in 5
793 mL LB while shaking at 250 rpm. This starter culture was then used to inoculate 0.5 L cultures.
794 Cultures were grown overnight in 2 L baffled flasks in Terrific Broth medium (Fisher Scientific)
795 supplemented with 4 g/L glycerol at 18°C while shaking at 250 rpm. Once the OD_{600} reached
796 approximately 1, expression was induced with 500 μM isopropyl β-D-1-thiogalactopyranoside

797 (IPTG). The pET vectors used contained a kanamycin resistance gene; kanamycin was used at
798 concentrations of 50 µg/mL in cultures[85]. After overnight expression at 18 ˚C, bacterial cells were
799 pelleted by centrifugation at 4100 x g at 10 ˚C. Pellets were resuspended in lysis buffer (1 M NaCl,
800 20 mM Tris, 20 mM imidazole, EDTA-free protease inhibitor, pH 7.5) and lysed by sonication while
801 on ice. Lysate was clarified by centrifugation at 25000 x g for 30 minutes at 10 ˚C. The clarified
802 lysate was then filtered with a 0.22 µm filter.

803 Proteins were purified using an AKTA Pure FPLC with 1 mL nickel-charged HisTrap
804 columns (Cytiva) for affinity chromatography of the His-tagged proteins. For N protein, after
805 injecting proteins onto the column, the column was washed with 15 column volumes of 3 M NaCl,
806 20 mM Tris, 20 mM imidazole, pH 7.5. For all other proteins, after injecting proteins onto the
807 column, the column was washed with 5 column volumes of 500 mM NaCl, 20 mM Tris, 20 mM
808 imidazole, pH 7.5. Proteins were eluted with a linear gradient up to 500 mM NaCl, 20 mM Tris,
809 500 mM imidazole, pH 7.5. Histidine tags were cleaved from the N protein using TEV protease
810 during dialysis. TEV protease was added to proteins and dialyzed overnight using 10 kDa MWCO
811 membranes (Slide-A-Lyzer G2, Thermo Fisher) into 300 mM NaCl, 20 mM Tris, 20 mM imidazole,
812 5mM DTT, pH 7.5 buffer at 4°C. The reaction mixture was purified using a nickel resin gravity
813 column (HisPur Ni-NTA Resin, Thermo Fisher) and the flow through was collected. Flow through
814 aliquots were concentrated and buffer exchanged into storage buffer (300mM NaCl, 20 mM Tris-
815 HCl, pH 7.5) using a 10kDa MWCO centrifugal filter (Amicon Ultra, Sigma). Proteins were either
816 reserved for the phosphorylation protocol or snap frozen in liquid N_2 in single-use aliquots and
817 stored at -80 °C.

818 **SDS-PAGE**

819 For chromatographically purified proteins, SDS-PAGE was run using NuPAGE 4-12% Bis-
820 Tris gels (Invitrogen) and stained using a Coomassie stain (GelCode Blue Safe Protein, Thermo
821 Scientific).

822 **Fluorescent labeling of N protein**

823 Purified N protein was dialyzed into PBS buffer with 0.1 mL sodium bicarbonate per 1 mL
824 protein solution. Protein was then labeled by adding a 3:1 molar ratio of Alexa 647 NHS ester
825 (Fisher Scientific) stored in DMSO. The mixture was incubated at 4°C for 1 h with rocking.
826 Unbound dye was removed by size exclusion chromatography (Superdex 200 Increase 10/300
827 GL, Cytiva). For phase separation assays, percent of dyed protein was adjusted to 5% of total by
828 dilution with undyed protein.

829 **Phosphorylation protocol**

830 ~80 μM N protein was prepared in a buffer containing 300 mM NaCl, 20 mM Tris, 1mM
831 dithiothreitol (DTT), 10 mM $MgCl_2$, and 2 mM ATP in a 200 μL reaction mixture. 5 μL GSK-3β and
832 5 μL SRPK (SignalChem Biotech) were added to the mixture. After incubation at 37°C for 120 min,
833 phosphorylation was confirmed using a SuperSep Phos-tag acrylamide gel (FujiFilm Wako
834 Chemicals). Enzymes were removed from the reaction mixture using GST-based affinity
835 chromatography. Briefly, 1 mL of gluthathione resin (Glutathione Sepharose 4B, Cytiva) was
836 packed in a gravity column. The column was washed with 300mM NaCl, 20mM Tris, pH 7.5 buffer.
837 The 200 uL of reaction mixture was diluted to a total of 2 mL using wash buffer and poured into
838 the column. The column flow through was collected. The column was washed with an additional
839 1 mL of wash buffer, which were collected. The flow through and wash fractions were combined
840 and the 3 mL of solution containing phosphorylated N protein was concentrated and buffer
841 exchanged using an Amicon Ultra 0.5 mL 10K MWCO centrifugal filter, according to manufacturer
842 instructions.

843 **RNA In vitro transcription protocol**

844 RNA production was carried out according to established protocols[86]. Templates were
845 gifted from the Gladfelter lab where they were synthesized (IDT) and cloned into pJet
846 (ThermoFisher Scientific K1231) plasmids using blunt end cloning. Directionality and sequence
847 were confirmed using Sanger sequencing (Azenta). Plasmids were linearized and then amplified
848 using PCR. 10 ng of plasmid was used as starting material and primers are noted in the

849 Supplemental Materials. Melting temperatures for the 1-1000 and N fragments were 69˚C. 5 µL
850 of PCR product was loaded onto an agarose gel to determine size and purity using SYBR™ Gold
851 Nucleic Acid Gel Stain (Invitrogen) and 1 kb Plus DNA Ladder (New England Biolabs). If the PCR
852 product was pure then the sample was purified (NEB DNA Clean-up kit). 100 ng of purified DNA
853 was used as a template for *in vitro* transcription (New England Biolabs) carried out according to
854 the manufacturer's instructions. Following incubation at 37°C for 18 h, *in vitro* transcription
855 reactions were treated with DNAse (New England Biolabs) according to the manufacturer's
856 instructions. Following DNAse treatment, reactions were purified with an RNA purification kit (NEB
857 T2040L). Purified RNA was verified for purity and size using an agarose gel and RNA Gel Loading
858 Dye (NEB B0363S) and RiboRuler High Range RNA Ladder (Thermo Scientific SM183).
859 Concentration was measured using a Nanodrop One spectrophotometer (ThermoFisher
860 Scientific).

861 Fluorescently labeled RNA was gifted by the Gladfelter lab. Cy3 RNA was transcribed from
862 the same template used above and using the same protocol described above, but with the addition
863 of 0.1 µL of Cy3 labeled UTP to each reaction (Sigma PA53026).

864 **Microscopy**

865 For microscopy experiments, protein samples were prepared as follows: N or pN protein
866 aliquots were thawed at room temperature. Proteins were then diluted and mixed with RNA (if
867 any) to obtain a final solution with 40 µM protein and 300 nM viral RNA or 1 mg/mL polyrA (unless
868 otherwise noted) and buffer conditions of 20 mM Tris-HCl, 150 mM NaCl, pH 7.5. Protein
869 concentrations were measured based on their absorbance at 280 nm using a Nanodrop
870 spectrophotometer (ThermoFisher).

871 Protein samples were plated on 1.5 thickness slides that were coated with 5% Pluronic F-
872 127 (Sigma-Aldrich) for a minimum of 10 minutes. The slides were washed with buffer solution
873 prior to plating the protein samples. A silicone spacer (0.5 mm) and a microfluidic temperature

controller (Cherry Biotech) were attached to the slide and the temperature of the sample was set to 37˚C during observation.

Confocal imaging was performed on a Zeiss Axio Observer 7 inverted microscope equipped with an LSM900 laser scanning confocal module and employing a 63x/1.4 NA plan-apochromatic, oil-immersion objective. GFP was excited to fluoresce with a 488 nm laser, Cy3 and Alexa-567 with a 561 nm laser and Cy5 with a 630 nm laser. Confocal fluorescence images were captured using GaAsP detectors. Transmitted light images were collected with either the ESID module or an Axiocam 702 sCMOS camera (Zeiss), in both cases using a 0.55 NA condenser.

Droplet image analysis

Image analysis and data processing for Figures 2, 3 and 4A-C and Supplementary Figures 2 and 8B-C were performed in MATLAB R2023a. The fluorescence intensity profile of the condensates with fluorescently labeled proteins was measured by using the Hough Transform to identify droplet locations and drawing a line that spanned the droplet diameter plus 1/4th of a radius length in each direction across the droplets. Line-scan graphs were generated in MATLAB. Total intensity and partitioning graphs were generated in MATLAB. Condensate perimeter and area were calculated using MATLAB's inbuilt regionprops function.

Giant unilamellar vesicle electroformation

Giant unilamellar vesicles were prepared by electroformation[87]. Briefly, 20 uL of a lipid solution containing 60% DOPC, 25% DOPE, 10% DOPS, 5% DGS-NTA(Ni) in chloroform (Avanti Lipids) was prepared. ~10 µL lipid solution was spread onto indium tin oxide (ITO)-coated glasses and dried under vacuum for 12 h. The plates were assembled into a chamber with a Teflon spacer and the swelling solution (~1 mL of 300mM sucrose) was introduced. For electroformation, a sinusoidal electric field of 2.0 Vpp and 10 Hz was applied using a function generator for 2.5 h, after which the frequency was reduced to 5 Hz for 30 min. Osmolarity of the sucrose solution (301 ± 1 mOsM) was lower than the osmolarity of the condensate NaCl solutions (324 ± 1 mOsM) to

900 ensure vesicles were not too tense. The solution osmolarities were confirmed using a freezing-
901 point osmometer (Advanced Instruments model 3D3).

902 **Contact angles measurement and geometric factor calculation**

903 A detailed explanation of the contact angles used in this work has been published
904 elsewhere[39]. Briefly, we measured the three contact angles θ_c, θ_e, θ_i from fluorescent images of
905 GUVs and condensates (for samples with GFP) or from brightfield images (for samples without
906 GFP). From these angles, we calculated the geometric factor, Φ. From Mangiarotti et al., 2024,
907 when Φ = −1 there is complete wetting of the membrane by the condensate phase, while Φ = +1
908 corresponds to dewetting of the membrane by the condensate phase. The geometric factor, Φ, is
909 negative if the membrane prefers the condensate over the exterior buffer and positive otherwise[56].
910 We followed the same procedure to measure θ_{in}, the intrinsic contact angle.

911 **Fluorescence Recovery After Photobleaching**

912 Circular bleach regions of approximate radius R = 1 μm were drawn in the center of protein
913 droplets. Alexa-647 was imaged and bleached with a 640 nm laser. Cy3 was imaged and
914 bleached with a 561 nm laser. Recovery curves were fit to a single exponential recovery model
915 $f(t) = A * (1 - e^{-t/\tau})$ to calculate the recovery timescale, τ.

916 **Passive Microrheology**

917 Yellow–green carboxylate-modified polystyrene beads (0.5 μm diameter; FluoSpheres,
918 Invitrogen) were used for video particle-tracking (VPT) microrheology measurements. Each
919 sample was prepared by mixing protein and RNA to a final concentration of 40 μM protein and
920 300 nM viral RNA or 1 mg/mL polyrA in 150 mM NaCl, 20 mM Tris-HCl buffer, pH 7.5. Next, 50 μL
921 of the protein and RNA sample was mixed with 1 uL of a 1:100 dilution of the fluorescent tracer
922 bead solution and the sample was plated on a 1.5 thickness slide pre-treated with Pluronic F127.
923 The sample was covered with a CherryTemp microfluidic temperature controller chip and the
924 sample was set to 37 ˚C and incubated for 1 hour.

925 VPT measurements were conducted on a Zeiss Axio Observer 7 inverted microscope
926 equipped with an Axiocam 702 monochrome sCMOS camera (Zeiss), employing a 63x, 1.4-
927 numerical aperture plan-apochromatic oil-immersion objective. The microscope focus was
928 adjusted to the midsection of the protein droplets for VPT acquisition. Epifluorescence video
929 imaging was initiated at the 1-hour timepoint, with fluorescence excitation using a 475-nm light-
930 emitting diode (Colibri 7, Zeiss). Videos of the tracer beads diffusing within the condensate were
931 collected at 100 frames per second for 2,000 frames. Imaging was conducted at 37 ˚C. For each
932 sample, three independent samples were made on different days, and ~20 videos were collected
933 from each sample, with each video containing ~5–50 tracer beads. Viscosity data presented in
934 Fig. 4D - G and Supplementary Fig 8D - E are the average of these independent trials.

935 Data analysis was conducted using the open-source particle tracking package TrackPy
936 (v0.5.0)[88] in Python and customized as needed. The TrackPy particle tracking code was used to
937 analyze the collected videos, starting with extracting particle trajectories. The MSD was calculated
938 from the trajectories of individual beads, followed by calculating the ensemble-average MSD. To
939 remove the static error from the MSD curves for calculating viscosities, we corrected the
940 ensemble-average MSD by subtracting the noise floor from the MSD curves[89]. In general, the
941 ensemble-average MSD often scales as a power law with lag time τ, as given by

942 $$< r^2(\tau) > = 2dD\tau^{\alpha}$$

943 where d is the number of dimensions (here d = 2, because data collection and analysis were
944 conducted in the x–y plane), D is the diffusion coefficient, and α is the diffusivity exponent. For a
945 purely viscous fluid, the diffusivity exponent α is unity, and the Stokes-Einstein relation can be
946 used to calculate the viscosity[90]. The α values for all the condensates tested were in the range of
947 0.3–1.1. We therefore used the Generalized Stokes-Einstein Relation (GSER) to measure the
948 viscoelastic properties of the condensates[90]. The frequency dependent GSER in the Fourier
949 domain is represented by the following equation:

$$G^*(\omega) = G'(\omega) + iG''(\omega) = \frac{d\, k_B\, T}{3\pi a(i\omega) < \Delta r^2(\omega) >}$$

where G*(ω) is complex shear modulus, k_B is Boltzmann's constant, T is the temperature, a is the bead radius, G'(ω) and G" (ω) are the frequency-dependent storage (elastic) and loss (viscous) moduli, respectively , and $< \Delta r^2(\omega) >$ is the unilateral Fourier transform of the MSD. We use an algebraic approach proposed by Mason et al. to estimate the Fourier transform of the MSD, which approximates the local MSD as a power-law function[60]. The algebraic expression is given by the following equation:

$$|G^*(\omega)| = \frac{d\, k_B\, T}{3\pi a < \Delta r^2(\tau = 1/\omega) > \Gamma[1 + \alpha(\tau = 1/\omega)]}$$

$$G'(\omega) = |G^*(\omega)| \cos\left(\frac{\pi\alpha(\omega)}{2}\right)$$

$$G''(\omega) = |G^*(\omega)| \sin\left(\frac{\pi\alpha(\omega)}{2}\right)$$

where $\alpha(\tau) = d\ln\left(\Delta r^2(\tau)\right)/d\ln(\tau)$ is the local power law exponent describing the logarithmic slope of $\Delta r^2(\tau)$ at $\tau = 1/\omega$ and Γ is the Gamma function. Next, cubic spline interpolation fitting is used on the calculated G' and G" data to reduce measurement noise generated in the algebraic conversion[91]. We plot the fitted G' and G'' to identify the cross-over frequency, or the timescale at which the material transitions from an elastic-dominant to a viscous dominant regime. To extract the zero-shear viscosity from the viscoelastic moduli, we use the following equation:

$$\eta(\omega) = \frac{G''(\omega)}{\omega}$$

and obtain the limit of η(ω) at low frequencies[60]. The presented viscoelastic moduli and zero-shear viscosities are the average from multiple videos (at least n = 10) taken from 3 independent samples.

The noise floor of the 500 nm beads was measured by allowing a solution of beads in water to dry on the glass surface of a slide, resulting in beads adhered to the glass surface. We

acquired the trajectories of the beads adhered to the glass surface using the same parameters and experimental setup as used for VPT studies of the samples.

Micropipette aspiration

The micropipette aspiration experiments were carried out on a Ti2-A inverted fluorescence microscope (Nikon, Japan) equipped with a motorized stage and two motorized 4-axes micromanipulators (PatchPro-5000, Scientifica) and a multi-trap optical tweezers (Tweez305, Aresis, Slovenia) according to the protocol we reported previously[62,63]. An oil immersion objective (100X; NA 1.30; Nikon) was integrated with an objective heating collar (OKOlab) and temperature controller (OKOlab) for 37 °C measurements. Micropipettes were made by pulling glass capillaries using a pipette puller (PUL-1000, World Precision Instruments). The pipette tip was then cut to achieve an opening diameter ~5 μm. Subsequently, the pipette was bent to an angle of approximately 40° using a microforge (DMF1000, World Precision Instruments).

MPA experiments were carried out in glass-bottom dishes (ES56291, Azer Scientific, US) that were pre-treated with 5% Pluronic F-127 (P2443-250G, Sigma) for 10 minutes to prevent adhesion of condensates to the glass. The micropipette was filled with the same buffer used in microscopy experiments (150 mM NaCl, 20 mM Tris-HCl, pH 7.5) using a MICROFIL needle (World Precision Instruments). The filled micropipette was then mounted onto a micromanipulator. The rear end of the pipette was connected to an automatic pressure controller (Flow-EZ, Fluigent; Pressure resolution 1 Pa).

Optical tweezers were used to contact and merge droplets to achieve a large (> 5 μm) condensate for easier MPA measurements and analysis. A secondary micropipette was used to hold the condensate during MPA. To minimize sample evaporation, 1.5 mL Milli-Q water was added to the edge of the dish, and the dishes were covered with a thin plastic wrap with a ~2 mm hole for pipette insertion. We observed that in vitro condensates always wet the inner wall of uncoated micropipettes. Therefore, the analysis of the MPA data follows the protocol described in Roggeveen et al[63]. Briefly, normalized aspiration length (aspiration length, Lp, over the pipette

998 radius, Rp) was segmented according to the pressure steps. For each segment, the slope of a
999 linear fitting of $(Lp/Rp)^2$ vs. time is equal to the effective shear rate. Then, the slope of aspiration
1000 pressure vs. shear rate graph gives 4η.

1001 **Fluorescence Polarization**

1002 Fluorescence polarization measurements were performed on a Tecan Spark microplate
1003 reader in a 384-well black plate at 20°C. A monochromator set the excitation wavelength at 485
1004 nM and the emission wavelength at 535 nm, with a 20 nm bandwidth. Purified N or pN protein
1005 was serially titrated in 150 mM NaCl, 20 mM Tris-HCl, pH 7.5 buffer and incubated with a constant
1006 4 nM FAM-labeled RNA (Azenta) for 10 min at room temperature (20˚C) prior to measurement.

1007 The data was analyzed using Matlab V2023a, with a one-site binding curve (hyperbola)
1008 fitted to the data. K_D values from three experiments were averaged and the standard deviation
1009 calculated. Data was normalized by subtracting the initial polarization value from each dataset.
1010 The one-site binding equation utilized is $mP = \frac{mP_{Max} * [N]}{K_D + [N]}$, in which mP is the observed
1011 millipolarization, mP_{MAX} is the maximum polarization, [N] is the concentration of protein
1012 (unmodified or phosphorylated).

1013 **smFRET**

1014 Single-molecule fluorescence measurements were performed as described in Cubuk et
1015 al. 2021[8] with a Picoquant MT200 instrument (Picoquant, Germany). Briefly, FRET experiments
1016 were performed by exciting the donor dye with a laser power of ~100 μW (measured at the back
1017 aperture of the objective) at 488 nm wavelength. For pulsed interleaved excitation of donor and
1018 acceptor, we used a repetition rate of 20 MHz for the donor excitation and a delay of approximately
1019 25 ns for acceptor excitation. Acceptor excitation was achieved by using a white laser (SuperK
1020 Extreme, NKT Photonics, Denmark), filtered by a z582/15 band pass filter (Chroma). Acceptor
1021 excitation power was adjusted to match the acceptor emission intensity to that of the donor
1022 (between 50 and 70 μW). Single-molecule FRET efficiency histograms were acquired from

1023 samples with protein concentrations of 100 pM labeled protein and the population with
1024 stoichiometry corresponding to 1:1 donor:acceptor labeling was selected. Photon detection
1025 events were stored with 16 ps resolution.

1026 Proteins were designed and prepared as described in Cubuk et al. 2021[8]. Following
1027 preparation, protein for smFRET experiments was phosphorylated using the protocol described
1028 above, with the exception of the use of 200 mM β-mercaptoethanol instead of 5 mM DTT. All
1029 samples were prepared in 50 mM HEPES pH 7.4, 150mM KCl, 200 mM β-mercaptoethanol (for
1030 photoprotection), 0.001% Tween 20 (for limiting surface adhesion) unless otherwise stated. All
1031 measurements were performed in custom-made glass cuvettes coated with PEG. Each sample
1032 was measured for at least 30 min at room temperature (295 ± 0.5 K). Protein concentrations were
1033 (1) 100 pM labeled protein for the low concentrations or (2) 100 pM labeled protein + 1 μM
1034 unlabeled protein for high concentration for the full-length construct or (3) 100 pM labeled protein
1035 + 4 μM unlabeled protein for high concentration for N^{1-246}.

1036 Determination of root mean square inter-dye distances from mean FRET transfer
1037 efficiencies was conducted as described in Cubuk et al. 2024[92]. Briefly, the Gaussian chain model
1038 was employed in the conversion, which relies on a single parameter, the root-mean-squared inter-
1039 dye distance r=<R^2>$^{1/2}$. Estimates for this parameter were obtained by numerically solving: $< E >$
1040 $= \int_0^\infty E(R)P(R)dR$ where <E> is the mean transfer efficiency, *R* is the inter-dye distance, *P(R)*
1041 represents the Gaussian chain distribution, and *E(R)* is the Förster equation for the dependence
1042 of transfer efficiency on distance *R* and Förster radius R_0.

1043 **smFRET lifetime analysis**

1044 Analysis of fluorescence lifetime from mean FRET transfer efficiencies was conducted
1045 as described in Cubuk et al. 2024[71].

1046 **smFRET dimerization constant**

1047 Modeling of dimerization was conducted as described in Cubuk et al. 2024[71].

1048 **Small-Angle X-ray Scattering**

1049 Small-angle X-ray scattering (SAXS) measurements were made at 16-ID-C LIXS beamline
1050 (National Synchrotron Light Source II (NSLS-II), Brookhaven National Laboratory; 15.14 keV X-
1051 rays (λ= 0.8189 Å) and two Pilatus 1 M detectors). Samples were prepared by diluting protein into
1052 150mM NaCl, 20mM Tris-HCl buffer to the concentrations desired (0.5 mg/mL – 4 mg/mL). Data
1053 over a q range of 0.005–0.25 $Å^{-1}$ was analyzed. Background subtraction was done using the
1054 scattering from the storage buffer (150mM NaCl, 20mM Tris-HCl, pH 7.5) and by scaling the buffer
1055 and sample intensities at the $q \sim 2$ $Å^{-1}$ water peak.

1056 The data were analyzed in BioXTAS RAW 2.1 with ATSAS 3.0.4 to determine the radius
1057 of gyration (R_g) by Guinier analysis, the compactness of the particle by Kratky plots and pair-
1058 distance distribution functions, $P(r)$. R_g from $P(r)$ was compared with the Guinier R_g to ensure
1059 internal consistency in data analyses. D_{max} was calculated from $P(r)$. Bead model reconstructions
1060 using a dummy atom model were obtained from the $P(r)$ functions generated and stored as .out
1061 files using GNOM in BioXTAS RAW 2.1 using the SAXS data as input. Bead models were
1062 generated using the DAMMIN program in the ATSAS 3.0.4 software package assuming single-
1063 phase objects.

1064 **LC-MS**

1065 Whole Protein: A sample with protein at a concentration of 10 μM was dissolved in 50%
1066 ammonium acetate solution and diluted 1:10 fold. The sample was then transferred into an LC
1067 vial. Reverse phase liquid chromatography (RPLC) was performed on an Acquity column BEH -
1068 C4 -300A, 1.7 micron (300 μm x 100 mm, Waters Corporation). Column temperature was set at
1069 40C. The following mobile phases were used A: Water with 0.1% formic acid; B: acetonitrile with
1070 0.1% formic acid. The M-Class micro flow LC (Waters Instruments) was operated at a flow rate
1071 of 8 μL/min, and 5 μL of sample was injected with an autosampler after equilibration of the
1072 column. For the separation of proteins, the following concentration gradients were used: starting
1073 with 5 – 90% B for 55 minutes and then back to 5% B for minutes 55 - 62. Prior to injection on

1074 the RPLC column, a blank run was performed. ESI-MS experiments were performed using a
1075 quadrupole-TWIMS-TOF hybrid mass spectrometer (Synapt G2 HDMS; Waters Corporation) in
1076 positive ionization mode with m/z scan range 400 - 4000. The applied experimental parameters
1077 were capillary voltage, 3.0 kV; sampling cone voltage, 40 V; source offset 80C; source
1078 temperature, 100C; desolvation temperature 250C; cone gas 50 L/Hr and desolvation gas 600
1079 L/Hr. Data analysis was performed using MassLynx 4.1 and protein deconvolution was
1080 performed using Mas Ent 1.

1081 Pepsin Digest: For pepsin digestion, protein samples were prepared with 2 µL of protein
1082 and 38 µL PBS and 60 µL of denaturation buffer (2 M urea, 20 mM TCEP, 0.8% formic acid).
1083 Samples were injected into a Vanquish LC system coupled to a Q Exactive HF mass
1084 spectrometer and digested online using a protease type XVIII/pepsin column (NovaBioassays).
1085 Peptides were first trapped on a Waters BEH C18 trap column (2.1 mm × 2 cm), then separated
1086 on a Hypersil Gold C18 analytical column (2.1 mm × 5 cm, 1.9 µm particle size) using a multi-
1087 step gradient at 5 °C: 0–4 min at 2% B, ramping to 10% B in 0.3 min, followed by 10% to 40% B
1088 over 7.6 min. MS data were acquired at 120,000 resolution over a 300–2000 m/z range. The top
1089 20 most intense precursor ions were selected for fragmentation using HCD (collision energy
1090 27), with MS/MS scans acquired at 15,000 resolution and a dynamic exclusion of 20 seconds.
1091 Data were analyzed in Proteome Discoverer 3.0 using Sequest HT against a custom database
1092 containing target proteins and kinases. Precursor and fragment mass tolerances were set to
1093 ±10 ppm and ±0.02 Da, respectively. N-terminal acetylation was set as a dynamic protein
1094 terminus modification, while methionine oxidation and phosphorylation at serine, threonine, and
1095 tyrosine were set as dynamic modifications. A non-specific protease setting was used. Peptide-
1096 spectrum matches were validated using the Fixed Value PSM Validator (maximum delta CN
1097 < 0.05), and phosphosite confidence was assessed with PhosphoRS.

1098 Trypsin Digest: Tryptic digests were prepared using the Single-Pot Solid-Phase-
1099 enhanced Sample Preparation (SP3) method with 10 µg of protein per sample. Following protein

binding and washing, digestion was initiated, and after 30 minutes at 37 °C, 20 µL was removed, acidified with 1 µL of 10% formic acid, and stored at −80 °C. The remaining sample was incubated overnight at 37 °C to complete digestion. Peptides from each timepoint were prepared for LC-MS/MS by mixing 10 µL of digest with 10 µL of 0.1% TFA (1:1), resulting in a final concentration of 0.1 µg/µL. From this, 5 µL (0.5 µg) was injected into a Q Exactive HF mass spectrometer using a 70-minute data-dependent acquisition (DDA) method. MS/MS data were searched against a protein database using MSFragger.

BS3 Cross-linking Experiment

Protein (2-10 µM in PBS at pH 7.5) was chemically cross-linked with bis(sulfosuccinimidyl) suberate (BS3) (Thermo Fisher) (50 µM) at room temperature for 30 min and quenched by adding Tris (pH 7.5) to a 20 mM final concentration. Reaction mixtures were then analyzed by SDS-PAGE.

Molecular dynamics simulations

All molecular dynamics (MD) simulations were performed using OpenMM 7.6.0[93] in the NVT ensemble. We simulated single truncated monomers, or full dimers of the N-protein using Langevin dynamics at a constant temperature of 310 K, with a friction coefficient of 0.01 ps^{-1} and an integration time step of 10 fs. Each system was enclosed in a cubic periodic box with periodic boundary conditions. Each chain was simulated for 260 ns, including a 10 ns equilibration phase followed by 250 ns of production dynamics. From the resulting trajectories, the first 50 ns of simulation were discarded as additional equilibration time before analysis.

Force field and interaction potentials:

We employed the HPS-Urry coarse-grained energy model[74], which includes bonded interactions, non-bonded interactions, and an elastic network model (ENM) for structured regions. The total interaction energy U_{total} is given by:

$$U_{total} = \sum_{i>j} \phi_{ij}^{elec} + \sum_{i>j} \phi_{ij}^{HPS} + \sum_{i=1}^{N-1} k_b\left(r_{i,i+1} - r_0\right)^2 + \sum_{(i,j)\in pairs} \frac{1}{2} k_d (r_{ij} - r_0^{(ij)})^2$$

where ϕ_{ij}^{elec} represents electrostatic interactions, ϕ_{ij}^{HPS} denotes hydrophobic interactions, and the third term models bonded interactions between adjacent residues using a spring constant $k_b = 20\,kj/\text{Å}^2$ and an equilibrium bond length r_0 = 3.82 Å. The last term corresponds to the elastic network model (ENM) which restrains the folded domains and is defined below.

Hydrophobic interactions are modeled using the Ashbaugh-Hatch potential[94]:

$$\phi_{ij}(r) = \begin{cases} \phi_{ij}^{LJ}(r) + (1-\lambda_{ij})\epsilon, & for\ r \leq 2^{1/6}\sigma_{ij}, \\ \lambda_{ij}\phi_{ij}^{LJ}(r), & for\ > 2^{1/6}\sigma_{ij} \end{cases}$$

with the Lennard-Jones potential defined as:

$$\phi_{ij}^{LJ}(r) = 4\epsilon\left[\left(\frac{\sigma_{ij}}{r}\right)^{12} - \left(\frac{\sigma_{ij}}{r}\right)^{6}\right]$$

In this, ϵ = 0.2 kcal/mol. λ_{ij} and σ_{ij} can be calculated by the arithmetic average of hydrophobicity values ($(\lambda_{ij} = \lambda_i + \lambda_j)/2$) and size ($(\sigma_{ij} = \sigma_i + \sigma_j)/2$), where σ_i and λ_i are the size and stickiness respectively of each amino acid type. Values of λ come from the Urry hydropathy scale[74,95], and σ from the predicted volume of amino acid residues[96].

Electrostatics are modeled using a Debye–Hückel potential[97]:

$$\phi_{ij}^{el}(r) = \frac{q_i q_j}{4\pi D r} e^{-\kappa r}$$

where q_i represents the charge of residue 'i' located at the center of the corresponding bead. D is the dielectric constant of the solvent, and κ is the inverse Debye screening length. For our calculations, we set D = 80, the dielectric constant of water, and κ = 1 nm^{-1}, which corresponds to salt concentrations of approximately 100 mM.

Elastic Network Model (ENM) for Folded domains:

To maintain structural integrity of folded domains, we applied an elastic network model (ENM) using a harmonic potential between non-bonded residue pairs within a cutoff distance based on the reference PDB structure[98]. The ENM potential is defined as:

$$u_{ENM}(r) = \sum_{(i,j)\in\, pairs} \frac{1}{2} k_d \left(r_{ij} - r_0^{(ij)}\right)^2$$

where r_{ij} is the current distance between two beads, r_0^{ij} is the reference distance between residues i and j from the crystal structure, and k_d is the force constant. For structured domains, each bead was placed at the center of mass calculated from all atoms in a residue (COM representation), while for intrinsically disordered domains, each bead was placed at the C_α atom position as has been used in similar models[75]. This model ensures that secondary and tertiary structures within folded domains remain stable throughout the simulation. Non-bonded interactions, including Ashbaugh-Hatch and Debye- Hückel potentials, are excluded for pairs restrained by the ENM.

The Pair Distance Distribution Function (PDDF) P(r) for each model was calculated by finding the cartesian distance between all residue pairs i,j. Contact between residues was defined as any 2 residues that were less than 1 nm apart, while ignoring interactions with itself, and 2 subsequent residues in sequence. Finally, a Bayesian Maximum Entropy ensemble reweighting scheme was implemented to adjust the statistical weights of the simulated conformations according to Lima Costa and Fushman et al[76].

1163 **References**

1164 1. Kim, D. *et al.* The Architecture of SARS-CoV-2 Transcriptome. *Cell* **181**, 914-921.e10
1165 (2020).

1166 2. McBride, R., van Zyl, M. & Fielding, B. C. The coronavirus nucleocapsid is a
1167 multifunctional protein. *Viruses* vol. 6 2991–3018 (2014).

1168 3. Perdikari, T. M. *et al.* SARS-CoV-2 nucleocapsid protein phase-separates with RNA and
1169 with human hnRNPs. *EMBO J.* **39**, 1–15 (2020).

1170 4. Korn, S. M., Dhamotharan, K., Jeffries, C. M. & Schlundt, A. The preference signature of
1171 the SARS-CoV-2 Nucleocapsid NTD for its 5'-genomic RNA elements. *Nat. Commun.* **14**,
1172 1–17 (2023).

1173 5. Roden, C. A. *et al.* Double-stranded RNA drives SARS-CoV-2 nucleocapsid protein to
1174 undergo phase separation at specific temperatures. *Nucleic Acids Res.* **50**, 8168–8192
1175 (2022).

1176 6. Ye, Q., West, A. M. V., Silletti, S. & Corbett, K. D. Architecture and self-assembly of the
1177 SARS-CoV-2 nucleocapsid protein. *Protein Sci.* **29**, 1890–1901 (2020).

1178 7. Morse, M., Sefcikova, J., Rouzina, I., Beuning, P. J. & Williams, M. C. Structural domains
1179 of SARS-CoV-2 nucleocapsid protein coordinate to compact long nucleic acid substrates.
1180 *Nucleic Acids Res.* **51**, 290–303 (2023).

1181 8. Cubuk, J. *et al.* The SARS-CoV-2 nucleocapsid protein is dynamic, disordered, and
1182 phase separates with RNA. *Nat. Commun.* **12**, 1–17 (2021).

1183 9. Zeng, W. *et al.* Biochemical characterization of SARS-CoV-2 nucleocapsid protein.
1184 *Biochem. Biophys. Res. Commun.* **527**, 618–623 (2020).

1185 10. Ribeiro-Filho, H. V. *et al.* Structural dynamics of SARS-CoV-2 nucleocapsid protein
1186 induced by RNA binding. *PLoS Comput. Biol.* **18**, 1–30 (2022).

1187 11. Tung, H. Y. L. & Limtung, P. Mutations in the phosphorylation sites of SARS-CoV-2
1188 encoded nucleocapsid protein and structure model of sequestration by protein 14-3-3.
1189 *Biochem. Biophys. Res. Commun.* **532**, 134–138 (2020).

1190 12. Wu, C. *et al.* Characterization of SARS-CoV-2 nucleocapsid protein reveals multiple
1191 functional consequences of the C-terminal domain. *iScience* **24**, 102681 (2021).

1192 13. Bouhaddou, M. *et al.* The Global Phosphorylation Landscape of SARS-CoV-2 Infection.
1193 *Cell* **182**, 685-712.e19 (2020).

1194 14. Wu, C. H. *et al.* Glycogen synthase kinase-3 regulates the phosphorylation of severe
1195 acute respiratory syndrome coronavirus mucleocapsid protein and viral replication. *J.*
1196 *Biol. Chem.* **284**, 5229–5239 (2009).

1197 15. Fung, T. S. & Liu, D. X. Post-translational modifications of coronavirus proteins: roles and
1198 function. **13**, 405–430 (2018).

1199 16. Patton, D., Stohlman, S. A., Fleming, J. & Lai, A. M. C. Synthesis and Subcellular
1200 Localization of the Murine Coronavirus Nucleocapsid Protein. *Virology* **130**, 527–532
1201 (1983).

1202 17. Yaron, T. M. *et al.* Host protein kinases required for SARS-CoV-2 nucleocapsid
1203 phosphorylation and viral replication. *Sci. Signal.* **15**, 1–16 (2022).

1204 18. Ino, Y. *et al.* Phosphopeptide enrichment using Phos-tag technology reveals functional
1205 phosphorylation of the nucleocapsid protein of SARS-CoV-2. *J. Proteomics* **255**, 104501
1206 (2022).

1207 19. Carlson, C. R. *et al.* Phosphoregulation of Phase Separation by the SARS-CoV-2 N

1208 Protein Suggests a Biophysical Basis for its Dual Functions. *Mol. Cell* **80**, 1092-1103.e4
1209 (2020).

1210 20. Ju, X. *et al.* A novel cell culture system modeling the SARS-CoV-2 life cycle. *PLoS*
1211 *Pathog.* **17**, 1–23 (2021).

1212 21. Syed, A. M. *et al.* SARS-CoV-2 evolution balances conflicting roles of N protein
1213 phosphorylation. *SSRN-Unpublished* 7–11 (2023) doi:10.1371/journal.ppat.1012741.

1214 22. Wu, C. H., Chen, P. J. & Yeh, S. H. Nucleocapsid phosphorylation and RNA helicase
1215 DDX1 recruitment enables coronavirus transition from discontinuous to continuous
1216 transcription. *Cell Host Microbe* **16**, 462–472 (2014).

1217 23. Peng, T. Y., Lee, K. R. & Tarn, W. Y. Phosphorylation of the arginine/serine dipeptide-rich
1218 motif of the severe acute respiratory syndrome coronavirus nucleocapsid protein
1219 modulates its multimerization, translation inhibitory activity and cellular localization. *FEBS*
1220 *J.* **275**, 4152–4163 (2008).

1221 24. Scherer, K. M. *et al.* SARS-CoV-2 nucleocapsid protein adheres to replication organelles
1222 before viral assembly at the Golgi/ERGIC and lysosome-mediated egress. *Sci. Adv.* **8**,
1223 (2022).

1224 25. Wolff, G. *et al.* A molecular pore spans the double membrane of the coronavirus
1225 replication organelle. *Science (80-.).* **369**, 1395–1398 (2020).

1226 26. Savastano, A., Ibáñez de Opakua, A., Rankovic, M. & Zweckstetter, M. Nucleocapsid
1227 protein of SARS-CoV-2 phase separates into RNA-rich polymerase-containing
1228 condensates. *Nat. Commun.* **11**, (2020).

1229 27. Chen, H. *et al.* Liquid–liquid phase separation by SARS-CoV-2 nucleocapsid protein and
1230 RNA. *Cell Res.* **30**, 1143–1145 (2020).

1231 28. Wang, S. *et al.* Targeting liquid–liquid phase separation of SARS-CoV-2 nucleocapsid
1232 protein promotes innate antiviral immunity by elevating MAVS activity. *Nat. Cell Biol.* **23**,
1233 718–732 (2021).

1234 29. Zhao, M. *et al.* GCG inhibits SARS-CoV-2 replication by disrupting the liquid phase
1235 condensation of its nucleocapsid protein. *Nat. Commun.* **12**, 1–14 (2021).

1236 30. Iserman, C. *et al.* Genomic RNA Elements Drive Phase Separation of the SARS-CoV-2
1237 Nucleocapsid. *Mol. Cell* **80**, 1078-1091.e6 (2020).

1238 31. Roden, C. A. *et al.* Double-stranded RNA drives SARS-CoV-2 nucleocapsid protein to
1239 undergo phase separation at specific temperatures. *Nucleic Acids Res.* **50**, 8168–8192
1240 (2022).

1241 32. Lasker, K. *et al.* The material properties of a bacterial-derived biomolecular condensate
1242 tune biological function in natural and synthetic systems. *Nat. Commun.* **13**, 5643 (2022).

1243 33. Yamasaki, A. *et al.* Liquidity Is a Critical Determinant for Selective Autophagy of Protein
1244 Condensates. *Mol. Cell* **77**, 1163-1175.e9 (2020).

1245 34. Kota, D. & Zhou, H.-X. Macromolecular Regulation of the Material Properties of
1246 Biomolecular Condensates. *J. Phys. Chem. Lett.* 5285–5290 (2022)
1247 doi:10.1021/acs.jpclett.2c00824.

1248 35. Carlson, C. R. *et al.* Phosphorylation modulates liquid-liquid phase separation of the
1249 SARS-CoV-2 N protein. *bioRxiv* 1–31 (2020) doi:10.1101/2020.06.28.176248.

1250 36. Carlson, C. R. *et al.* Reconstitution of the SARS-CoV-2 ribonucleosome provides insights
1251 into genomic RNA packaging and regulation by phosphorylation. *J. Biol. Chem.* **298**,
1252 102560 (2022).

1253 37. Yuan, F. *et al.* Membrane bending by protein phase separation. *Proc. Natl. Acad. Sci. U.*
1254 *S. A.* **118**, (2021).

1255 38. Agudo-Canalejo, J. *et al.* Wetting regulates autophagy of phase-separated compartments
1256 and the cytosol. *Nature* **591**, 142–146 (2021).

1257 39. Mangiarotti, A., Chen, N., Zhao, Z., Lipowsky, R. & Dimova, R. Wetting and complex
1258 remodeling of membranes by biomolecular condensates. *Nat. Commun.* **14**, 1–15 (2023).

1259 40. Scherer, K. M. *et al. SARS-CoV-2 nucleocapsid protein adheres to replication organelles*
1260 *before viral assembly at the Golgi/ERGIC and lysosome-mediated egress*. *Sci. Adv* vol. 8
1261 https://www.science.org (2022).

1262 41. Klein, S. *et al.* SARS-CoV-2 structure and replication characterized by in situ cryo-
1263 electron tomography. *Nat. Commun.* **11**, (2020).

1264 42. Collins, L. T. *et al.* Elucidation of SARS-Cov-2 Budding Mechanisms through Molecular
1265 Dynamics Simulations of M and E Protein Complexes. *J. Phys. Chem. Lett.* **12**, 12249–
1266 12255 (2021).

1267 43. van Meer, G. Membrane lipids, where they are and how they behave: Sphingolipids on
1268 the move. *FASEB J.* **24**, 112–124 (2010).

1269 44. Pramanik, S., Steinkühler, J., Dimova, R., Spatz, J. & Lipowsky, R. Binding of His-tagged
1270 fluorophores to lipid bilayers of giant vesicles. *Soft Matter* **18**, 6372–6383 (2022).

1271 45. Verheije, M. H. *et al.* The Coronavirus Nucleocapsid Protein Is Dynamically Associated
1272 with the Replication-Transcription Complexes. *J. Virol.* **84**, 11575–11579 (2010).

1273 46. Zimmermann, L. *et al.* SARS-CoV-2 nsp3 and nsp4 are minimal constituents of a pore
1274 spanning replication organelle. *Nat. Commun.* **14**, (2023).

1275 47. Klatte, N., Shields, D. C. & Agoni, C. Modelling the Transitioning of SARS-CoV-2 nsp3
1276 and nsp4 Lumenal Regions towards a More Stable State on Complex Formation. *Int. J.*
1277 *Mol. Sci.* **24**, (2023).

1278 48. Hurst, K. R., Koetzner, C. A. & Masters, P. S. Characterization of a Critical Interaction
1279 between the Coronavirus Nucleocapsid Protein and Nonstructural Protein 3 of the Viral
1280 Replicase-Transcriptase Complex. *J. Virol.* **87**, 9159–9172 (2013).

1281 49. Hurst, K. R., Ye, R., Goebel, S. J., Jayaraman, P. & Masters, P. S. An Interaction
1282 between the Nucleocapsid Protein and a Component of the Replicase-Transcriptase
1283 Complex Is Crucial for the Infectivity of Coronavirus Genomic RNA. *J. Virol.* **84**, 10276–
1284 10288 (2010).

1285 50. Ni, X., Han, Y., Zhou, R., Zhou, Y. & Lei, J. Structural insights into ribonucleoprotein
1286 dissociation by nucleocapsid protein interacting with non-structural protein 3 in SARS-
1287 CoV-2. *Commun. Biol.* **6**, (2023).

1288 51. Zhang, Z. *et al.* Structure of SARS-CoV-2 membrane protein essential for virus assembly.
1289 *Nat. Commun.* **13**, (2022).

1290 52. He, R. *et al.* Characterization of protein-protein interactions between the nucleocapsid
1291 protein and membrane protein of the SARS coronavirus. *Virus Res.* **105**, 121–125 (2004).

1292 53. Lu, S. *et al.* The SARS-CoV-2 nucleocapsid phosphoprotein forms mutually exclusive
1293 condensates with RNA and the membrane-associated M protein. *Nat. Commun.* **12**,
1294 (2021).

1295 54. Klein, S. *et al.* SARS-CoV-2 structure and replication characterized by in situ cryo-
1296 electron tomography. *Nat. Commun.* **11**, 1–10 (2020).

1297 55. Bergner, T. *et al.* Near-Native Visualization of SARS-CoV-2 Induced Membrane

Remodeling and Virion Morphogenesis. *Viruses* **14**, 1–17 (2022).

56. Mangiarotti, A., Schmidt, K. V., Lipowsky, R. & Dimova, R. Lipid packing and cholesterol content regulate membrane wetting by biomolecular condensates. *bioRxiv* 1–31 (2024).

57. Pinto, A. L. *et al.* Ultrastructural insight into SARS-CoV-2 entry and budding in human airway epithelium. *Nat. Commun.* **13**, 1–14 (2022).

58. Saud, Z. *et al.* The SARS-CoV2 envelope differs from host cells, exposes procoagulant lipids, and is disrupted in vivo by oral rinses. *J. Lipid Res.* **63**, 100208 (2022).

59. Ma, W., Zheng, G., Xie, W. & Mayr, C. In vivo reconstitution finds multivalent RNA–RNA interactions as drivers of mesh-like condensates. *Elife* **10**, 1–32 (2021).

60. Mason, T. G. Estimating the viscoelastic moduli of complex fluids using the generalized Stokes-Einstein equation. *Rheol. Acta* **39**, 371–378 (2000).

61. Wang, Z., Lou, J. & Zhang, H. Essence determines phenomenon: Assaying the material properties of biological condensates. *Journal of Biological Chemistry* vol. 298 (2022).

62. Wang, H., Kelley, F. M., Milovanovic, D., Schuster, B. S. & Shi, Z. Surface tension and viscosity of protein condensates quantified by micropipette aspiration. *Biophysical Reports* vol. 1 (2021).

63. Roggeveen, J. V., Wang, H., Shi, Z. & Stone, H. A. A calibration-free model of micropipette aspiration for measuring properties of protein condensates. *Biophys. J.* **123**, 1393–1403 (2024).

64. Alshareedah, I., Moosa, M. M., Pham, M., Potoyan, D. A. & Banerjee, P. R. Programmable viscoelasticity in protein-RNA condensates with disordered sticker-spacer polypeptides. *Nat. Commun.* **12**, 1–14 (2021).

65. Laghmach, R. *et al.* RNA chain length and stoichiometry govern surface tension and stability of protein-RNA condensates. *iScience* **25**, (2022).

66. Iserman, C. *et al.* Genomic RNA Elements Drive Phase Separation of the SARS-CoV-2 Nucleocapsid. *Mol. Cell* **80**, 1078-1091.e6 (2020).

67. Lorenz, R. *et al.* ViennaRNA Package 2.0. *Algorithms Mol. Biol.* **6**, 122–128 (2011).

68. Demchenko, A. . Fluorescence Polarization and Rotational Mobility. in *Ultraviolet Spectroscopy of Proteins* 198–207 (Springer, 1986).

69. Svergun, D. I. & Koch, M. H. J. Small-angle scattering studies of biological macromolecules in solution. *Reports Prog. Phys.* **66**, 1735–1782 (2003).

70. Kikhney, A. G. & Svergun, D. I. A practical guide to small angle X-ray scattering (SAXS) of flexible and intrinsically disordered proteins. *FEBS Lett.* **589**, 2570–2577 (2015).

71. Cubuk, J. *et al.* The dimerization domain of SARS CoV 2 Nucleocapsid protein is partially disordered as a monomer and forms a high affinity dynamic complex. *bioRxiv* (2024).

72. Ghosh, L. S. K. A theoretical method to compute sequence dependent configurational properties in charged polymers and proteins. *J. Chem. Phys* **143**, (2015).

73. Dignon, G. L., Zheng, W., Kim, Y. C., Best, R. B. & Mittal, J. Sequence determinants of protein phase behavior from a coarse-grained model. *PLoS Comput. Biol.* **14**, 1–23 (2018).

74. Regy, R. M., Thompson, J., Kim, Y. C. & Mittal, J. Improved coarse-grained model for studying sequence dependent phase separation of disordered proteins. *Protein Sci.* **30**, 1371–1379 (2021).

75. Cao, F., Bülow, S. von, Tesei, G. & Lindorff-Larsen, K. A coarse-grained model for

disordered and multi-domain proteins. *bioRxiv* 2024--02 (2024) doi:10.1002/pro.5172.

76. Gama Lima Costa, R. & Fushman, D. Reweighting methods for elucidation of conformation ensembles of proteins. *Curr. Opin. Struct. Biol.* **77**, 102470 (2022).

77. Bernetti, M., Hall, K. B. & Bussi, G. Reweighting of molecular simulations with explicit-solvent SAXS restraints elucidates ion-dependent RNA ensembles. *Nucleic Acids Res.* **49**, (2021).

78. Botova, M. *et al.* A specific phosphorylation-dependent conformational switch of SARS-CoV-2 nucleoprotein inhibits RNA binding. *Sci. Adv.* (2024) doi:10.1126/sciadv.aax2323.

79. Stuwe, H. *et al.* Phosphorylation in the Ser/Arg-rich region of the nucleocapsid of SARS-CoV-2 regulates phase separation by inhibiting self-association of a distant helix. *J. Biol. Chem.* **300**, 107354 (2024).

80. Liu, X. *et al.* Targeting the Coronavirus Nucleocapsid Protein through GSK-3 Inhibition. *medRxiv* 2021.02.17.21251933 (2021).

81. Mohandas, D. V. & Dales, S. Endosomal association of a protein phosphatase with high dephosphorylating activity against a coronavirus nucleocapsid protein. *FEBS Lett.* **282**, 419–424 (1991).

82. Vögele, J. *et al.* High-resolution structure of stem-loop 4 from the 5′-UTR of SARS-CoV-2 solved by solution state NMR. *Nucleic Acids Res.* **51**, 11318–11331 (2023).

83. Tugaeva, K. V. *et al.* The Mechanism of SARS-CoV-2 Nucleocapsid Protein Recognition by the Human 14-3-3 Proteins :SARS-CoV-2 N association with host 14-3-3 proteins. *J. Mol. Biol.* **433**, 166875 (2021).

84. Tugaeva, K. V. *et al.* Human 14-3-3 Proteins Site-selectively Bind the Mutational Hotspot Region of SARS-CoV-2 Nucleoprotein Modulating its Phosphoregulation. *J. Mol. Biol.* **435**, 167891 (2023).

85. Studier, F. W. Stable Expression Clones and Auto-Induction for Protein Production in E. coli. in *Methods in molecular biology (Clifton, N.J.)* vol. 1091 17–32 (2014).

86. Langdon, E. M. *et al.* mRNA structure determines specificity of a polyQ-driven phase separation. **1**, 922–927 (2018).

87. Angelova, M. I. & Dimitrov, D. S. Liposome Electro formation. 303–311 (1986).

88. Allan, D. B., Thomas, C., Keim, N. C., van der Wel, C. M. & Verweij, R. W. soft-matter/trackpy: Trackpy. (2021).

89. McGlynn, J. A., Wu, N. & Schultz, K. M. Multiple particle tracking microrheological characterization: Fundamentals, emerging techniques and applications. *J. Appl. Phys.* **127**, (2020).

90. Furst EM, S. T. *Microrheology*. (Oxford University Press, 2017). doi:10.1093/oso/9780199655205.001.0001.

91. Tassieri, M., Evans, R. M. L., Warren, R. L., Bailey, N. J. & Cooper, J. M. Microrheology with optical tweezers: Data analysis. *New J. Phys.* **14**, (2012).

92. Cubuk, J. *et al.* The disordered N-terminal tail of SARS-CoV-2 Nucleocapsid protein forms a dynamic complex with RNA. *Nucleic Acids Res.* **52**, 2609–2624 (2024).

93. Eastman, P. *et al.* OpenMM 7: Rapid development of high performance algorithms for molecular dynamics. *PLoS Comput. Biol.* **13**, 1–17 (2017).

94. Ashbaugh, H. S. & Hatch, H. W. Natively Unfolded Protein Stability as a Coil-to-Globule Transition in Charge/Hydropathy Space. *JACS* 9536–9542 (2008).

95. Urry, D. W. *et al.* Hydrophobicity scale for proteins based on inverse temperature transitions. *Biopolymers* **32**, 1243–1250 (1992).

96. Kim, Y. C. & Hummer, G. Coarse-grained Models for Simulations of Multiprotein Complexes: Application to Ubiquitin Binding. *J. Mol. Biol.* **375**, 1416–1433 (2008).

97. Debye, P. & Huckel, E. De la theorie des electrolytes. i. abaissement du point de congelation et phenomenes associes. *Phys. Zeitschrift* **24**, 185–206 (1923).

98. Bahar, I., Atilgan, A. R. & Erman, B. Direct evaluation of thermal fluctuations in proteins using a single-parameter harmonic potential. *Fold. Des.* **2**, 173–181 (1997).